Analysis of Hybrid Satellite-to-Satellite Tracking and Quantum Gravity Gradiometry Architecture for Time-Variable Gravity Sensing Missions

by

Mitchell David Rosen

THESIS

Presented to the Faculty of the Graduate School of

The University of Texas at Austin

in Partial Fulfillment

of the Requirements

for the Degree of

MASTER OF SCIENCE IN ENGINEERING

THE UNIVERSITY OF TEXAS AT AUSTIN

August 2021

Analysis of Hybrid Satellite-to-Satellite Tracking and Quantum Gravity Gradiometry Architecture for Time-Variable Gravity Sensing Missions

APPROVED BY

SUPERVISING COMMITTEE:

Srinivas Bettadpur, Supervisor

Himanshu Save

Dedicated to my parents for their constant love and support

Acknowledgments

First and foremost, I would like to thank my advisor Dr. Srinivas Bettadpur. Throughout my graduate studies and research funded by JPL SURP grant 1656926, he has been incredibly kind, helpful and patient - all of which was key to the completion of this study. I am endlessly grateful to him for taking me under his wing. My thanks go out to Sheng-wey Chiow and Nan Yu from JPL, whose insight were key to the construction of this study. I would also like to thank Furun Wang for the inestimable help he's provided me with while creating and running simulations for this study and Geethu Jacob for the crucial help creating plots and analyzing data. My thanks go out to others at the Center for Space Research, including Dr. Steven Poole and Dr. Peter Nagel for providing me with constant advice and troubleshooting, and Dr. Himanshu Save for serving as the second reader for this thesis. Additionally, thank you to the Texas Advanced Computing Center (TACC) whose resources made this study possible.

My thanks to all of the friends that helped keep me afloat when finishing this thesis seemed impossible - I could not have completed this without them. Finally, thank you to my wonderful family, who have always provided the support necessary to help me reach my goals.

Analysis of Hybrid Satellite-to-Satellite Tracking and Quantum Gravity Gradiometry Architecture for Time-Variable Gravity Sensing Missions

Mitchell David Rosen, M.S.
The University of Texas at Austin, 2021

Supervisor: Srinivas Bettadpur

The Gravity Recovery and Climate Experiment (GRACE) mission, its follow on (GRACE-FO) and the Gravity-field and steady-state Ocean Circulation Experiment (GOCE) mission have been key contributors to the advancement of the study of Earth's gravity field in the 21^{st} century. The gravity gradiometers on GOCE are limited in their sensitivity and are therefore limited to studying the Earth's static gravity field. However, recent advancements in atomic interferometry have increased the feasibility of implementing this technology to the study of time-variable aspects of the Earth's gravity field, as with the GRACE satellite-to-satellite tracking technology. It is anticipated that these measurement types will provide information about the time-variable gravity field at different wavelengths, and as such a hybrid architecture mission implementing both has been presented. A measurement proof of concept

study is performed for this proposed architecture, analyzing the possible improvements over current best time-variable gravity models at mid and small spatial scales and the effects of prominent sources of error.

A series of simulations is performed through an orbit that is nearly polar, nearly circular, with an altitude of 450 km and the satellites spaced 220 km apart. The noises present in the gradiometer and pointing knowledge, which serves as a second form of gradiometer error, are tested in combination at varying levels to gain insight into their impact upon the accuracy of the resulting estimated gravity field. The impact of aliasing error upon this hybrid architecture is also tested and analyzed. The results demonstrate clear improvement over the GRACE-FO architecture when the gradiometer noise is sufficiently small. Even at the largest gradiometer noise levels, the inclusion of the gravity gradient data greatly reduces the impact of aliasing error. At varying noise levels, it is shown that either the gradiometer or attitude determination system can become the limiting factor of the architecture.

This analysis serves to quantify the improvements in gravity field recovery a hybrid architecture can create with both current and under-development technologies.

Table of Contents

List of Tables

List of Figures

Chapter 1

Introduction

1.1 Background

There are few, if any, known life forms that can persist without liquid water. Liquid water is believed to be so integral to life, its presence is one of the first criteria astronomers look for when searching for other planets with the potential for hosting life [5]. We define our ecosystems by how much water they contain, and build cities and civilizations around waterways. But water also has the potential to take life. Powerful storms and large floods devastate cities, taking and ruining countless lives. For all of these reasons, working to an understanding of the water cycle has been of constant importance since ancient times. Hebrew Scholars observed in Ecclesiastes 1:6-7 that, despite all rivers flowing into the sea, the sea never seemed to fill. In the Ramayana, further understanding of the water cycle is shown through speculation that water is heated by the sun before being sent back to the surface as rain [6]. The study of the water cycle has, of course, developed significantly since these observations were made. In 1580, Bernard Palissy became the first to assert, rightfully, that springs and rivers must be completely dependent upon rainwater (as opposed to underground channels that brought seawater inland) [7]. In the early 20^{th} century, Sir Gilbert Walker provided, among other things, an explanation for

the El Niño-Southern Oscillation Phenomenon [8].

A vast array of improvements in the study of the movement of water across the Earth were made in the 20^{th} century. While the field at large is worthy of further discussion, this study will focus more narrowly on the significant developments made with the advent of space based experimentation in the late 20^{th} and early 21^{st} centuries. Satellite laser ranging missions such as LAGEOS and the Gravity Recovery and Climate Experiment (GRACE) and gravity gradient missions such as the Gravity-field and steady-state Ocean Circulation Experiment (GOCE) have shown that improved understanding of time-variations in the water cycle lead to a broader understanding of the processes taking place within our planet writ large [9, 10]. Continued effort to understand the water cycle by carrying on the work of these missions with improved instruments will further our ability to understand and address planetary problems, such as global climate change.

1.2 Previous Studies

Gravitational force exerted by objects upon each other depends upon the objects' potential, which in turn is determined by the mass and the distribution of that mass within the objects. Therefore, as the distribution of mass in and on the Earth changes, the geopotential and the gravitational field around Earth change as well. Various processes cause such changes - shifting tectonic plates, atmospheric wind patterns, melting ice sheets and, principally, the hydrological cycle. Weather events that move large amounts of water, such

as rain runoff in the Amazon and monsoon season in southeast Asia, have large notable impacts upon the Earth's gravity field. Due to this direct connection, measuring the Earth's gravity field leads to important insights into the water cycle. Geopotential measurements can be collected either from the surface or from space. Surface based gravimeters are accurate but expensive and cumbersome, thus make them difficult for use in collecting measurements over large areas and large periods of time [11]. Satellite based gravimetry, while also expensive, offers the ability to cover the entire surface of the Earth regularly in short periods of time. Many satellite missions have been developed in the past 50 years dedicated solely to furthering our understanding of the Earth's geopotential and, by extension, the water cycle.

The Laser Geodynamics Satellite (LAGEOS) 1, launched by NASA in 1976, was the first satellite ever launched for the explicit purpose of satellite laser ranging; it's successor mission, LAGEOS 2, was launched in 1992. Both satellites are completely passive, covered in 426 cube corner reflectors used for ground based laser ranging. Laser ranging technology improved drastically in the first 15 years of LAGEOS, with associated precision decreasing from approximately a meter in 1976 to 10 mm in 1991 [12]. These missions made many contributions to the understanding of geophysical perturbations that act on objects in orbit around Earth; however, large scale improvements in tracking capabilities in the early years of these missions did not change the simplicity of the satellites themselves, capable of no more than providing a point for tracking from the ground. Spatial resolution of gravity field models

created with data from the LAGEOS missions was limited to the hemispheric scale, and the temporal resolution limited the study of time variable gravity to secular changes and seasonal variations in J_2 [13]. The Challenging Mini-satellite Payload (CHAMP) mission, launched only two years before the GRACE mission in 2000, was a single satellite that proved the viability of precise electrostatic accelerometers for the removal of non-gravitational effects on the orbital motion; this use of accelerometers, as well as the use of GPS receivers and the "Small Sat" design, were adopted by the GRACE mission, which quickly changed the paradigm of gravity sensing from space [14].

The GRACE missions - the Gravity Recovery and Climate Experiment (GRACE) launched in 2002 and GRACE Follow-On (GRACE-FO) launched in 2018 - marked a significant step forward in gravity sensing from space. GRACE provided, for the first time, data sensitive enough to allow scientists to map the Earth's gravitational field at a spatial resolution of 300 km. The first GRACE mission consisted of two satellites in the same orbit tracking each other through low-low satellite-to-satellite tracking (LL SST) using K-band ranging (KBR), tracked from the ground through SLR and tracked from GPS satellites above via high-low (HL) SST. The information gathered by GRACE allowed for the monitoring of many causes of subtle changes in the gravitational field over 15 years, such as glacial ice loss, terrestrial water storage and ocean bottom pressure [1]. Data recorded by GRACE led to the construction of monthly gravity fields with geoid height accuracy of 2-3 mm at spatial scales greater than 600 km and annual gravity fields with the

same accuracy at spatial scales greater than 400 km. However, monthly mean gravity fields were shown to be impacted by aliasing error, introduced through short-period atmosphere, ocean and continental hydrology variations. This requires de-aliasing with approximate models of the mass variability, reducing but not eliminating aliasing error, with the benefits clearest at middle and high spherical harmonic degrees [15]. A study done by Kurtenbach et al. was able to use information from prior hydrological models of the Earth's gravity field to establish temporal correlation patterns in the Earth's gravity field, which they then used to create single day models of the Earth's gravity field [16]. There is some sense in utilizing temporal correlations for certain applications of GRACE data, such as the long term study of patterns in glacial mass. However, it is not possible to model variations at these short time scales reliably with current hydrological models; models of much higher fidelity than currently exist would be needed to properly de-alias the results of extremely small time scale variations. While it may be possible to do so with tracking data from other satellites, this method has not been successfully applied to date. Thus, while Kurtenbach's methodology is sound, current technology is not sufficient for its application.

The GRACE-FO mission has largely the same architecture as the original GRACE mission, with each of the instruments on board being updated to modern standards. The only major difference between the two missions is the addition of a laser ranging interferometer (LRI), which measures the distance between the satellites in parallel with the K-band instrument on board. The

LRI - designed to be 26 times as precise as the KBR instrument that was on GRACE - was expected to lead to improved accuracy in recovered gravity fields [1]. These instruments are compared against each other by the average size of their post-fit residuals, the differences between their collected data and the corresponding values predicted by the gravity field estimated using that data. GRACE-FO KBR post-fit residuals are on average approximately half the magnitude of GRACE KBR post-fit residuals, and the average GRACE-FO LRI post-fit residuals are approximately half the size of KBR residuals. The LRI field estimates themselves show little overall improvement over those estimated with KBR data - this is due to both short-period variations that are currently not covered by de-aliasing models and the accelerometer becoming the limiting error source [17]. The GRACE-FO mission - which has by all accounts been a success - was mandated by NASA under funding from the Climate Continuity Initiative, whose directive was to continue "as-is" for the extension of data records [18].

The GOCE mission, launched in 2009, was the first to use a gravity gradiometer to observe the Earth's gravity field from space [19]. The gradiometer on the GOCE mission was composed of three pairs of electrostatic accelerometers. This gradiometer had a sensitivity of 1 mE (or $10^{-12}\ \frac{\frac{m}{s^2}}{m}$) in two axes with the third axis being slightly less sensitive. This gradiometer, considered to be high performing at the time, was far less sensitive than the atom interferometric gradiometer to be discussed in this study. It reached the level necessary for the GOCE missions to complete the assigned mission, but would not be suffi-

cient for a time variable gravity mission. Of note is the choice, during a 1998 review, to utilize the accelerometer based gradiometer over another type which required cryogenic cooling to 2 K, was considered to be too heavy and had less development maturity at the time [20]. The method by which this other gradiometer worked is not made clear; however, it is likely the case that an early version of an atom interferometry gradiometer was briefly under consideration for use on the GOCE mission. It is true, however, that this technology was far less developed at the time. The sensitivity of the electrostatic accelerometer based gradiometer was adequate for the mission designers as they were seeking only to model the Earth's static gravity field, not time variations which are mostly on a scale smaller than the sensitivity of the instrument. However, a processing guide published several years following the launch of the mission details the practice of taking into account and eliminating from the GOCE results the effects of both tidal and non-tidal gravity field time variations. The data used to make these corrections come from various different models and GRACE data [21]. This practice demonstrates the expectation on the part of the researchers that gravity gradient measurements are capable of detecting temporal variations in the gravity field.

In the time since GOCE was launched, data analyses have shown repeatedly the usefulness of gravity gradiometry data. Modeling with GOCE data (supplemented by GRACE data at low degrees) is shown to be reliably more accurate at 145 degrees [22]. Various studies involving data from both the GRACE and GOCE missions have shown that gravity field modelling ben-

efits from the presence of both SST and gravity gradient data. Farahani et al. demonstrated the superiority of models utilizing both types of data to models utilizing GRACE data only. This was confirmed via the comparison of mean ocean dynamic topography models, derived from the static gravity field models, against an independent, state-of-the-art mean ocean dynamic topography model and the ability of the models to predict future GRACE and GOCE data. These mixed models are also shown to compare favorably with EGM2008, particularly in areas with poor terrestrial gravimetry coverage, though not at high (above 200) spherical harmonic degrees [23]. The aforementioned sensitivity of the GOCE gradiometer to time variable gravity signals was applied by Rexer et al. [10] to be capable of rendering a reduction in striping in GRACE monthly and bi-monthly solutions. This effect was only achievable while applying both types of data (gradiometry and GPS) from GOCE, with the effect focused on spherical harmonic degrees 45-60. However, they do admit that they were only able to prove this application of the GOCE data in months with relatively weak performance by GRACE at and above degree 45; the possibility of this application of GOCE data in this manner during other time periods is speculated but left to further study [10]. The suggestion that gradiometry data of limited sensitivity from GOCE, in combination with GPS data, has the potential to consistently improve GRACE solutions implies that a single hybrid mission capable of collecting low-low satellite-to-satellite tracking, gravitational gradiometry at an improved sensitivity level and GPS data together could be the logical next step in space based gravity sensing.

This expectation paired nicely with the knowledge that gravity gradient data outperforms SST at middle and high harmonic degrees. Given this knowledge and the search, as outlined in the Decadal survey [24], for a mission architecture that can improve upon the capabilities of GRACE and GRACE-FO, this study into a hybrid SST-QGG gravity sensing mission was initiated.

1.3 Mission Overview

The GRACE missions, representing the most recent advancement in gravity sensing missions, made use of more advanced architecture capabilities. The GRACE architecture utilizes a constellation of two satellites in the same orbit, separated by 220 $\pm$ 50 km [1]. The satellites fly in a circular near-polar orbit with altitude of approximately 500 km [25]. Due to this flying formation, mass variations in the Earth have slightly different impacts on the orbits of the two satellites, depending on the distance at a given moment from a mass variation to each of the satellites. There are known variations, accounted for in existing gravity field models, and anomalies, variations that affect the satellites which are not accounted for by current gravity field models. Anomalies can be caused by misunderstood or completely unknown structures on or within the Earth, an unknown material composition, an unknown density, or any such gap in knowledge used to create a gravity field model. As the lead satellite approaches a variation, it will accelerate with respect to the rear satellite, causing the range and range-rate between the two satellites to change. Shortly thereafter, as the lead satellite orbits away from the variation and the rear

satellite approaches, the rear satellite will be subjected to an acceleration matching the one the lead satellite experienced just prior. As the satellites continue to orbit over various mass variations around the Earth, constantly varying accelerations result in constantly varying range and range-rate; this data, via a thorough estimation process, can used in tandem with GPS data to conclude the Earth's spherical harmonic gravity field over the time of data collection [26]. Known variations do not lead to new information; anomalies create data residuals, which in turn provide new information about the gravity field and the cause(s) of the anomalies.

Each satellite is equipped with a suite of identical instruments to make the necessary measurements. Included in that instrument suite on GRACE-FO are a dual frequency K/Ka band microwave ranging instrument (MWI) and laser ranging interferometer (LRI), both for tracking the inter-satellite range, three star camera sensors and an angular rate sensing inertial measurement unit (IMU) for attitude determination, a precise accelerometer at the satellite's center of mass for tracking non-gravitational forces and a GPS receiver for precise orbit determination (POD) [17, 3]. On GRACE-FO, to allow for orbit determination, the GPS receiver provides position and velocity data accurate within 20 cm and 0.1 $\frac{m}{s}$, respectively, at an update rate of 0.5 Hz with a pulse per second time signal accurate within 300 pico-seconds. The accelerometer is accurate on the scale of $10^{-10}\frac{m}{s^2}$ along the X axis and $10^{-12}\frac{m}{s^2}$ along the Y and Z axes, allowing for removal of non-conservative, non-gravitational forces such as solar and Earth radiation pressure, drag, etc. The star cameras provide

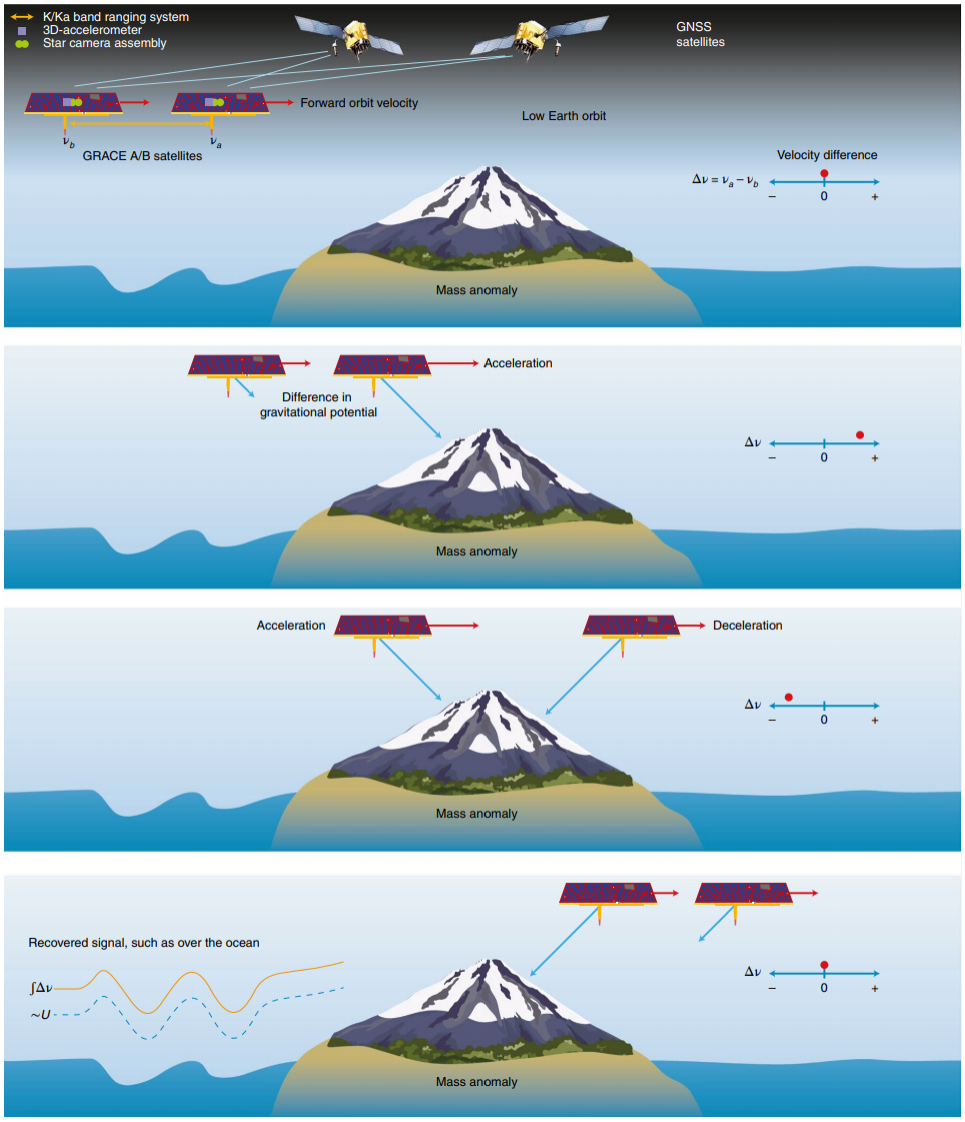

Figure 1.1: GRACE and GRACE-FO Architecture [1]

attitude information accurate on the order of 10 μRad.

On the architecture studied in this thesis, the instruments from GRACE-FO will be paired with an atom-interferometer (quantum) gravity gradiometer mounted to one of the two satellites in a hybrid architecture. All instruments will work in tandem to provide satellite to satellite tracking (SST) and quantum gravity gradients (QGG) caused by mass variations within the Earth. A gravity gradient is simply the gradient of the gravitational acceleration vector. As the gradient of a vector, gravity gradient data comes in the form of a dyad. These two data types, paired with GPS data, will be utilized by a weighted least-squares estimator. This process will produce high degree and order spherical harmonic gravity field solutions.

1.4 Thesis Objective and Outline

This study aims to validate the measurement concept of a hybrid QGG-SST mission and to show that it has the potential to improve upon the time-variable gravity field recovery sensitivity of the GRACE-FO mission, particularly at smaller spatial scales. Such a hybrid architecture advances the science objectives from the most recent Decadal Survey for Earth Science and Applications [24]. The Decadal Survey explores the needs of the Earth Science community then proceeds to list requirements for technological improvements that could be used to meet those needs. Improvements for gravity sensing at these smaller spatial scales allow for the application of the results of the mission to fields which are just out of reach for the GRACE missions, particularly

relevant to climate science, including hydrometeorology and ocean dynamics.

This validation is performed through a series of simulations of the hybrid architecture with various levels of instrument specifications. These simulations, performed with existing data analysis architecture at the Center for Space Research (CSR), present a strong set of tools for understanding the sensitivity of recovered gravity fields to a variety of different error sources all at once. For this ability to show interactions of the different error sources, simulations were chosen as the preferred method of validation over simple error propagation or covariance analyses. Preliminary tests were performed to understand which of these sources of error would be the most relevant to this study and therefore would be the focus of the study.

Through these preliminary studies it was shown that the primary error sources are the QGG sensitivity itself and the knowledge of the angular orientation and angular motion, which are vitally important to the usefulness of the QGG data. Error models are based upon currently existing and expected near future sensor capabilities. Aliasing errors and smoothing methods are also discussed; aliasing the limiting error source for the GRACE missions, warranting study of how it is affected by QGG data. An analysis is performed by varying these error levels to understand how they interact to set an expected overall sensitivity for the mission architecture.

Chapter 2 discusses the process for estimating Earth's gravity field. Non-gravitational forces are separated out so that gravitational forces may be related to Earth's potential and described in spherical harmonic models.

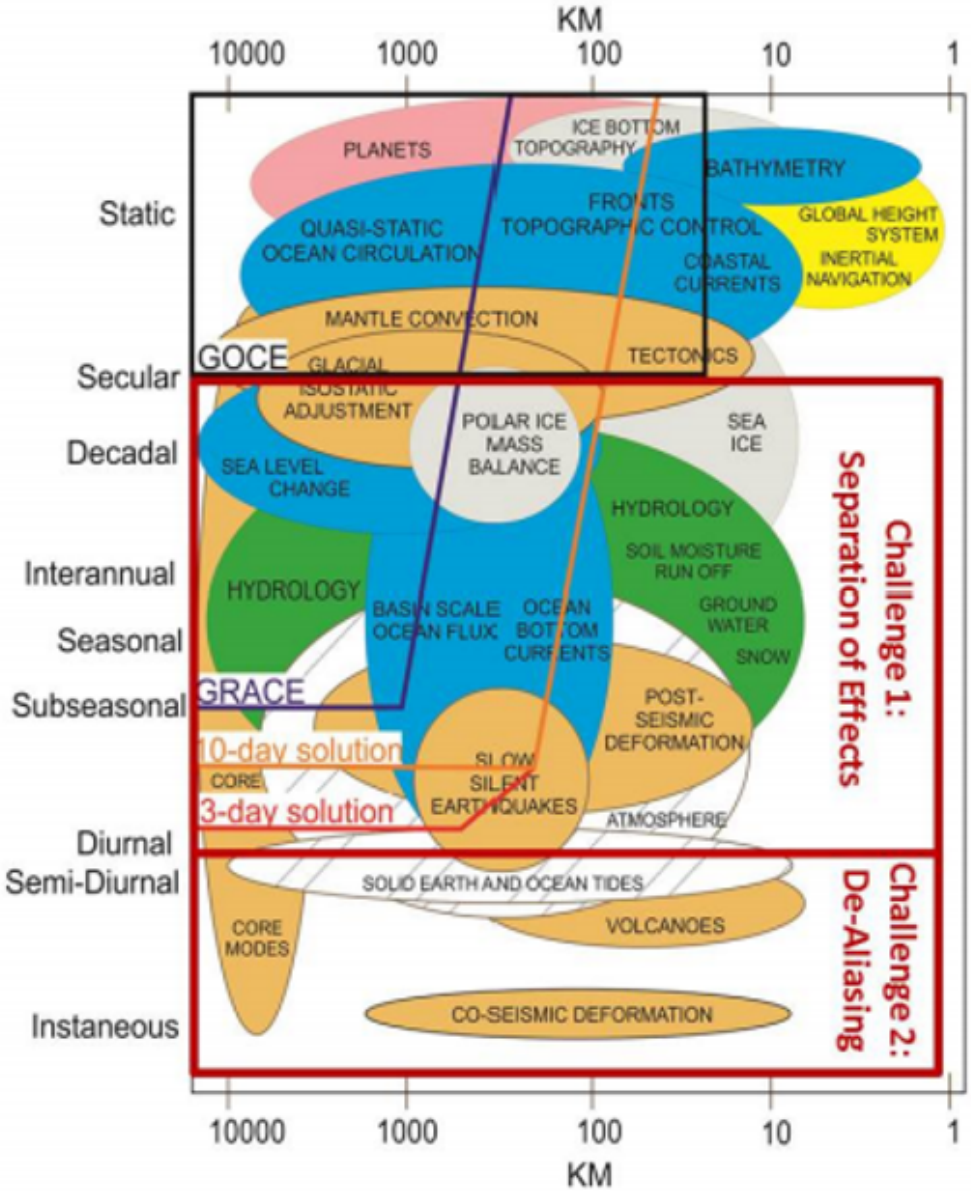

Figure 1.2: Spatio-Temporal Observation Requirements [2]

These force models are utilized in establishing equations of motion for the two satellites. These equations of motion are described in terms of the position and velocity of the satellites. The necessary observables for a hybrid architecture are range, range-rate and GPS measurements, as with the GRACE missions, and gravity gradient measurements. Application of these equations of motion, the orbit determination and least squares solution for estimating the Earth's gravity field is outlined.

Chapter 3 outlines the method by which the QGG collects data and the main error sources that impact the capabilities of the hybrid architecture, pointing knowledge and control and aliasing. The use of white noise in simulating the primary error sources is discussed as the method for investigating the robustness of the architecture as it exists in the simulations. With the pointing knowledge and control (via the star camera noise), the QGG precision and the de-aliasing methods tested, all other aspects of the simulated mission are maintained from the GRACE-FO mission.

Chapter 4 begins by describing the design of the parametric study conducted to determine the precision benefits of a hybrid architecture over the GRACE missions. The configuration for testing the hybrid architecture with different levels of the most vital error sources, as described in Chapter 3, is laid out. This study allows for determination of whether the hybrid architecture, generally, will lead to improvements over the GRACE missions. Additionally, it allows for an understanding of how the hybrid architecture will perform with various combinations of the levels of each of the pertinent error sources. In

Chapter 5, these findings are converted to conclusions about whether a mission with a hybrid architecture is recommended and, in the case that it is, what instrument sensitivities are needed.

Chapter 2

Gravity Field Estimation and Processing

2.1 Introduction

The range between the two satellites detected by the SST device and the gravity gradient detected by the QGG on the lead satellite are the two primary measurables for the hybrid time-varying gravity sensing mission. Numerical differentiation is used with the range data to acquire range-rate and range-acceleration information, while the accelerations caused by the gravity gradient tensor are isolated. These measurements, in combination with GPS tracking data, are the basis for gravity field estimation. The process for recovering a geopotential field from this data is rooted in the variational method for differential corrections. This study accesses that process by first simulating LL SST, QGG and GPS data in a 'true' gravity field. The simulated data is degraded with measurement and instrumentation noise to reach a data set similar to one which may be reported to ground by the satellites; the process to this point is accomplished through the Multi-Satellite Orbit Determination Process (MSODP), developed at the Center for Space Research at the University of Texas at Austin (CSR). This data set is then used by the AESoP, a parallel least squares estimator, to determine the gravitational field, which can then be compared to the 'truth' field used by the simulation and the results

of other similar simulations. The difference between the truth and estimated fields is an indication of the sensitivity of results to various causes of error.

This chapter will provide an abridged discussion of gravity field estimation theory. More detailed analyses of the process are provided by Kaula [27], Tapley [28] and Frommknecht [29]. An overview of the application of these theories in MSODP and AESoP is provided along with dicsussion of how the mission observables tie in with particular focus on the gravity gradient data. Full descriptions of MSODP and AESoP are provided by Rim [30], and Gunter, respectively [31].

2.2 Gravity Field Estimation Theory

2.2.1 Equations of Motion

For a near-Earth satellite, the equations of motion can be described in an inertial reference frame in the following manner [30]:

$$\ddot{\vec{r}} = \vec{a}_g + \vec{a}_{ng} + \vec{a}_{emp} \tag{2.1}$$

where

$\vec{a}_g$ is the sum of accelerations due to gravitational forces acting on the satellite

$\vec{a}_{ng}$ is the sum of accelerations due to non-gravitational forces acting on the surfaces of the satellite

$\vec{a}_{emp}$ is the sum of accelerations due to remaining unmodeled forces acting on the satellite due to an either incorrect or incomplete description of the forces acting on the satellite or the values of the parameters inherent to the description of those forces

The accelerometer, as mentioned in section 1.3, measures all of the non-gravitational forces that act on the satellite, hence the combination of all of those forces into one acceleration, $\vec{a}_{ng}$. The remainder of this section will focus on the gravitational forces. The gravitational forces acting on the satellite can be expressed via the following [30]:

$$\vec{a}_g = \vec{P}_{geo} + \vec{P}_{dtides} + \vec{P}_{otides} + \vec{P}_{rotdef} + \vec{P}_{nbody} + \vec{P}_{rel} \tag{2.2}$$

where

$\vec{P}_{geo}$ is perturbations due to the geopotential of the Earth

$\vec{P}_{dtides}$ is perturbations due to solid Earth tides

$\vec{P}_{otides}$ is perturbations due to ocean tides

$\vec{P}_{rotdef}$ is perturbations due to rotational deformation

$\vec{P}_{nbody}$ is perturbations due to Sun, Moon, planets

$\vec{P}_{rel}$ is perturbations due to relativity

Perturbing forces of the satellite due to the gravitational attraction of the Earth can be expressed as the gradient of the Earth's potential, which satisfies the Laplace equation, $\nabla^2 U = 0$ [30]:

$$\nabla U = \nabla(U_s + \Delta U_{st} + \Delta U_{ot} + \Delta U_{rd}) = \vec{P}_{geo} + \vec{P}_{dtides} + \vec{P}_{otides} + \vec{P}_{rotdef} \quad (2.3)$$

where U_s is the potential due to the solid-body mass distribution and the other values ΔU are the potential changes due to solid-body tides, ocean tides and rotational deformation, respectively. The perturbing potential of the solid-body mass distribution of the Earth is generally expressed in terms of a spherical harmonic expansion in a body fixed reference frame formulated in the following manner [27, 32]:

$$U_s(r, \phi, \lambda) = \frac{GM_e}{r} + \frac{GM_e}{r} \sum_{l=1}^{\infty} \sum_{m=0}^{l} \left(\frac{a_e}{r}\right)^l \bar{P}_{lm}(\sin\phi) \left[\bar{C}_{lm} \cos m\lambda + \bar{S}_{lm} \sin m\lambda\right] \quad (2.4)$$

where

GM_e is the Universal Constant of Gravitation times the mass of Earth

a_e is the mean equatorial radius of Earth

$\bar{P}_{lm}(\sin\phi)$ is the normalized associated Legendre function of degree l and order m

$\bar{C}_{lm}, \bar{S}_{lm}$ are the normalized Stokes spherical harmonic coefficients

r, λ, ϕ are the spherical coordinates where the potential is calculated

2.2.2 Orbital Models

The hybrid SST-QGG architecture has three main observables: the range measurements (which are differentiated into range-rate and range-acceleration), the GPS phase and pseudo-range and the QGG gravity gradient measurements. As with the GRACE missions, the range and GPS tracking data are utilized through phase double differences, the desired observable for generating simulations through MSODP.

The instantaneous LL SST range is determined in the terms of each satellite's position vector, as shown in equation 2.6 and figure 2.1; the line-of-site (LOS) unit vector is formulated via 2.7.

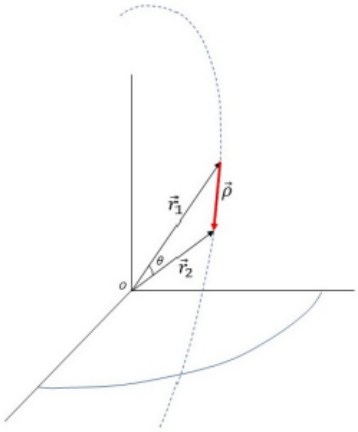

Figure 2.1: Satellite Range

$$\vec{\rho} = \vec{r}_1 - \vec{r}_2 \tag{2.5}$$

$$\rho = \sqrt{\vec{\rho} \cdot \vec{\rho}} \tag{2.6}$$

$$\hat{e}_\rho = \frac{\vec{\rho}}{\rho} \tag{2.7}$$

Twice differentiating the range yields the range-rate and range-acceleration, formulated in equations 2.8 and 2.9, respectively.

$$\dot{\rho} = \dot{\vec{\rho}} \cdot \hat{e}_\rho + \vec{\rho} \cdot \dot{\hat{e}}_\rho = \dot{\vec{\rho}} \cdot \hat{e}_\rho + \hat{e}_\rho \cdot \left[\dot{\vec{\rho}} - \dot{\rho} \cdot \hat{e}_\rho \right] = \dot{\vec{\rho}} \cdot \hat{e}_\rho \tag{2.8}$$

$$\ddot{\rho} = \ddot{\vec{\rho}} \cdot \hat{e}_\rho + \dot{\vec{\rho}} \cdot \dot{\hat{e}}_\rho \tag{2.9}$$

The range-acceleration equation, simplified with equation 2.7, yields the form in equation 2.10.

$$\ddot{\rho} = \ddot{\vec{\rho}} \cdot \hat{e}_\rho + \frac{1}{\rho} \left[|\dot{\vec{\rho}}|^2 - \dot{\rho}^2 \right] \tag{2.10}$$

With the equations for the range, range-rate and range-acceleration along the satellite's LOS defined in terms of the position vector of each satellite, the LL SST phase double difference can be calculated. GPS double differences are calculated via a process utilizing the ranges between two GPS satellites, a ground station and one of the hybrid architecture satellites in low Earth orbit (LEO). This process serves to eliminate errors, providing positioning

accuracy within 1 cm [33]. As this study is focused on the combined use of SST and QGG measurements, the derivation of these GPS measurements is not included. A detailed derivation is given by Rim [30].

2.2.3 Gravity Gradient Data Processing

The QGG collects and processes accelerations due to gravity gradient data in a manner similar to the GOCE mission. That process, as described in Frommknecht et al. [29], is outlined herein.

The QGG instrument collects accelerations at two locations (described in detail in section 3.3.1) separated by some distance. The final measurable output of the QGG, the total differential phase shift, is the difference between the accelerations at the two measurement points, which are formulated as follows.

$$\bar{a} \approx -\left(U - \Omega^2 - \dot{\Omega}\right) \cdot \bar{A} + \bar{D} \tag{2.11}$$

where

U is the gravity gradient tensor

Ω^2 is the square of the angular rates tensor

$\dot{\Omega}$ is the angular acceleration matrix

$\bar{A}$ is the vector from the origin of the QGG of the center of mass of the individual accelerometer

$\bar{D}$ is the vector of non-conservative accelerations acting on the satellite's center of mass

U, Ω and $\dot{\Omega}$ are of the forms described in equations 2.12 through 2.14.

$$U = \begin{bmatrix} U_{xx} & U_{xy} & U_{xz} \\ U_{yx} & U_{yy} & U_{yz} \\ U_{zx} & U_{zy} & U_{zz} \end{bmatrix} \tag{2.12}$$

$$\Omega^2 = \begin{bmatrix} -\omega_z^2 - \omega_y^2 & \omega_x\omega_y & \omega_x\omega_z \\ \omega_x\omega_y & -\omega_z^2 - \omega_x^2 & \omega_y\omega_z \\ \omega_x\omega_z & \omega_y\omega_z & -\omega_x^2 - \omega_y^2 \end{bmatrix} \tag{2.13}$$

$$\dot{\Omega} = \begin{bmatrix} 0 & -\dot{\omega}_z & \dot{\omega}_y \\ \dot{\omega}_z & 0 & -\dot{\omega}_x \\ -\dot{\omega}_y & \dot{\omega}_x & 0 \end{bmatrix} \tag{2.14}$$

where

$U_{ij} = \frac{\partial^2 U}{\partial x_i \partial x_j}$

ω_i is the angular rate of the satellite

The QGG observable is the difference between the accelerations at the two measurement points. As $\bar{A}$ represents the vector from the center of mass of the QGG, which is symmetrical, the vector $\bar{A}_i$ to one of the accelerometers is equal and opposite the vector $\bar{A}_j$ to the other. Therefore, the in line differential acceleration between the two accelerometers is of the following form.

$$\bar{a}_{d,ij} = \frac{1}{2}(\bar{a}_i - \bar{a}_j) = -(U - \Omega^2 - \dot{\Omega}) \cdot \bar{A}_i \tag{2.15}$$

Knowledge of the angular rates and angular acceleration allow for separating out their effects to isolate the acceleration due to the gravity gradient. With a single-axis gradiometer such as the one utilized by the hybrid architecture, it is necessary to collect this information independent of the gradiometer. The process for determining the angular accelerations, which necessary for deriving the angular rates and angular acceleration, is detailed by Frommknecht et al. [29].

2.3 Orbit Determination and Least Squares Solution

The simulation procedure is described herein; a more detailed description is given by Gunter [31]. The first step involves choosing a truth field, which will serve as the correct description of the Earth's gravity field in the simulation environment. All of the gravity fields estimated are compared back to this field. For this study, the GIF48.2000.GEO mean background gravity field was chosen as the truth. The field is complete to degree and order 360, but only information up to degree and order 120 is utilized in this study.

With the truth model and an initial condition, the ephemeris is derived by numerically integrating the position and velocity of the LEO satellites over the entire trajectory. Through this, MSODP generates a series of GPS, K/Ka band ranging (KBR) and QGG observations. Both the LL and HL SST measurements are treated through the variational method [34]. This method, as described by Bettadpur and McCullough [35] and shown through the following formulation, treats the difference between observations and expected values ex-

pected based on the truth gravity field as being due to variations in the state and parameters of the two LEO satellites from those expected values.

$$y(t) = O(r(t), \dot{r}(t), \beta) - C(r^*(t), \dot{r}^*(t), \beta^*) \tag{2.16}$$

where

O is observed data

C is data computed with best a priori models

$r(t)$ and $\dot{r}(t)$ are range and range-rate between the LEO satellites

β is observational parameters

* represents best known versions of the state and parameters based on the nominal model

The nominal model is a gravity field used by the software to prepare partials for estimation. Most simulations discussed in this study utilize the same gravity field for both the truth and nominal gravity fields. With this setup, the differences between O and C are known to be directly attributable to measurement noise. To model aliasing error, as discussed in 3.5, the truth and nominal models are made to differ.

Treating the range, range-rate and observational parameters as combinations of their best known values and variations from those values, equation 2.16 can be re-framed in the following manner with a mathematical model that converts state components and parameters to observations, G.

$$\begin{aligned} r(t) =& r^*(t) + \delta r(t) \\ \dot{r}(t) =& \dot{r}^*(t) + \delta \dot{r}(t) \\ \beta =& \beta^* + \delta\beta \end{aligned} \tag{2.17}$$

$$\begin{aligned} y(t) &= G(r^*(t) + \delta r(t), \dot{r}^*(t) + \delta\dot{r}(t), \beta^* + \delta\beta) - G(r^*(t), \dot{r}^*(t), \beta^*) \\ &= \frac{\partial G}{\partial r}\delta r(t) + \frac{\partial G}{\partial \dot{r}}\delta\dot{r}(t) + \frac{\partial G}{\partial \beta}\delta\beta \end{aligned} \tag{2.18}$$

At each time step up to the final observation time m, the observational residuals at each time step are expressed as follows.

$$\begin{aligned} y(t_1) &= \tilde{H}_{r_1^*}\delta r(t_1) + \tilde{H}_{\dot{r}_1^*}\delta\dot{r}(t_1) + \tilde{H}_{\beta^*}\delta\beta^* \\ &\vdots \\ y(t_k) &= \tilde{H}_{r_k^*}\delta r(t_k) + \tilde{H}_{\dot{r}_k^*}\delta\dot{r}(t_k) + \tilde{H}_{\beta^*}\delta\beta^* \\ &\vdots \\ y(t_m) &= \tilde{H}_{r_m^*}\delta r(t_m) + \tilde{H}_{\dot{r}_m^*}\delta\dot{r}(t_m) + \tilde{H}_{\beta^*}\delta\beta^* \end{aligned} \tag{2.19}$$

To reduce $y(t)$ to fewer parameters and establish an explicit dependence upon the force model parameters (the values of which will be estimated) a state transition matrix is created based on the assumption that $\delta r(t)$ and $\delta\dot{r}(t)$ must be dynamically consistent as a function of time. Thus, using the observational residuals at each time step, the data is now prepared for estimation [35].

The variational method is not necessary for data collected by the QGG. Rather, a direct parameter estimation method is permissible.

These observations have simulated measurement and instrument noise added to them. The noise models included in this simulation represent QGG measurement noise, star camera pointing knowledge and accelerometer error. Non-gravitational perturbation effects, including Earth and Solar radiation pressure and atmospheric drag, are introduced. MSODP then generates partials for all three data types with respect to the truth field, collected in Regres files. The least squares estimation process is then performed with AESoP, utilizing the generated observations and partials with optimal weighting implemented. This process is outlined in the following flow chart.

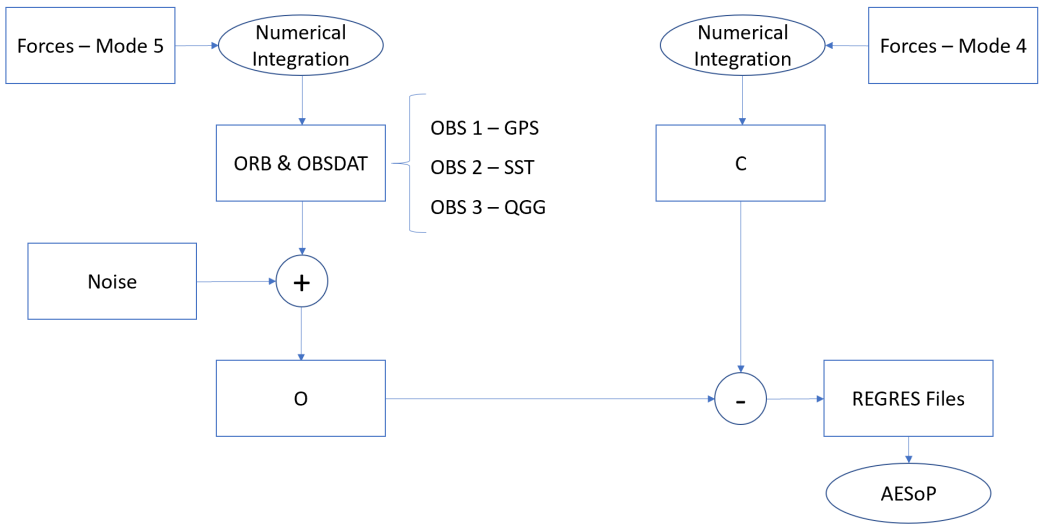

Figure 2.2: Least Squares Estimation Process Flowchart

Chapter 3

Satellite-to-Satellite and Gravity Gradient Measurements

3.1 Introduction

The hybrid SST-QGG architecture described and simulated in this study is intended to continue the work of the GRACE missions, adding the QGG technology to allow for higher sensitivity at smaller spatial scales. An understanding of the SST and QGG measurement methods and the errors accounted for in the simulation process is necessary for a proper evaluation of the simulation results. This chapter will provide an overview of these topics. Because the simulation specifications are based upon the instruments utilized by the GRACE-FO mission, an outline of the specifications of that instrument suite and the numerical methods for processing the SST data are given. The atom interferometer gravity gradiometer measurement methods, as described by Yu [4], are provided alongside the gravity gradient data processing formulation. Due to the focus of this study upon the impact of introducing a gradiometer measurements to the GRACE-FO architecture, a analysis of the GPS tracking measurement methods is forgone. An decsription of these measurements and their intrinsic errors is given by Kim [33].

The error sources which present the most immediate barriers to full utilization of the capabilities of the hybrid architecture, pointing knowledge and aliasing, are considered. Methods and architecture design choices for minimizing the effects of these error sources are given, and expected impacts of these error sources upon the final results despite these mitigation methods are discussed. This chapter will provide the context necessary to properly interpret the simulation results to follow.

3.2 Satellite to Satellite Measurement Process

The microwave ranging instrument (MWI) on each of the GRACE-FO satellites, shown in detailed schematic in figure 3.1, is used to collect SST measurements. This instrument consists of a K/Ka-band Ranging (KBR) Assembly, three GPS antennas operating at L1 and L2 GPS frequencies with associated low noise amplifiers (LNA), a redundant pair of Ultrastable Oscillators (USO) and a redundant pair of Instrument Processing Units (IPU). The KBR assembly, with a pair of redundant Microwave Assemblies (MWA) and a single horn antenna transmits signals to and receives signals from the sister satellite in the 24 GHz K-band and 32 GHz Ka-band [3].

As the the MWIs on the satellite pair are exact twins, on one satellite an interferometric beat note is utilized to create a phase offset between the incoming and outgoing signals, to allow for ease of distinguishing between signals. Measurements taken on the satellite receiving these offset signals account for this imposed phase shift [3].

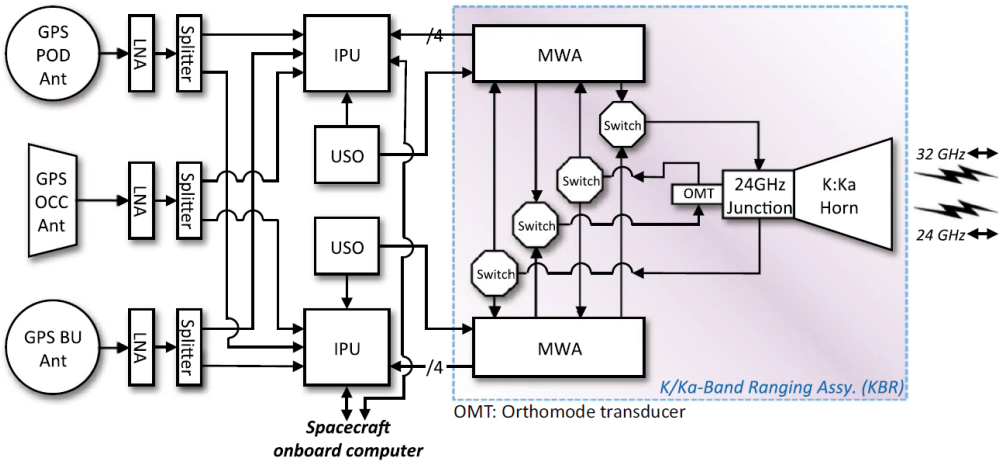

Figure 3.1: GRACE-FO Single Satellite MWI and GPS Antenna Block Diagram [3]

The LRI instrument, as discussed in section 1.2 and shown in detail in figure 3.2, is also used to collect SST measurements. On each satellite is a Triple Mirror Assembly (TMA), a laser source (LAS) and a laser frequency cavity assembly (CAV) and an optical bench assembly (OBA). The master spacecraft sends a frequency stabilized light beam to the distant satellite, which receives the signal and (similar to the MWI) uses an interferometric beat note to determine the phase offset between the incoming and local lasers. This is used to offset the local laser, which then sends a signal back to the master satellite. The master satellite then receives a signal which corresponds to the round trip distance between the two satellites.

The simulations in this investigation utilize simulated LRI data with an applied noise square-root power spectral density (PSD) of 0.08 $\mu m/\sqrt{Hz}$.

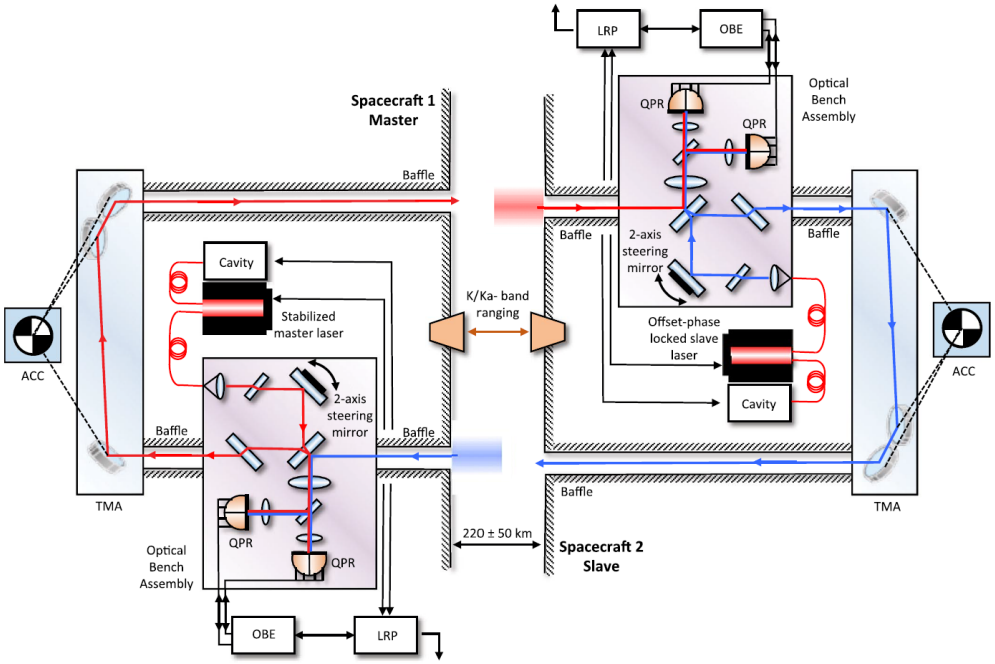

Figure 3.2: GRACE-FO Two Satellite LRI Block Diagram [3]

Detailed attention is not given to the fidelity of SST measurements as the study is intended only as a measurement proof of concept. In discussion in chapter 4, these measurements will be referred to simply as SST, with no distinction between MWI and LRI.

3.3 Atomic Interferometer Gradiometer

3.3.1 Measurement Process

An overview of the process by which the Atomic Interferometer Gradiometer collects gravity gradient data is presented by this section. A more complete description, lab setup and implementation are available in Yu, Ko-

hel et al. [4]. An expected accuracy range of the QGG given an extended interrogation time and gradiometer arm length were provided via private correspondence by Sheng-wey Chiow [36].

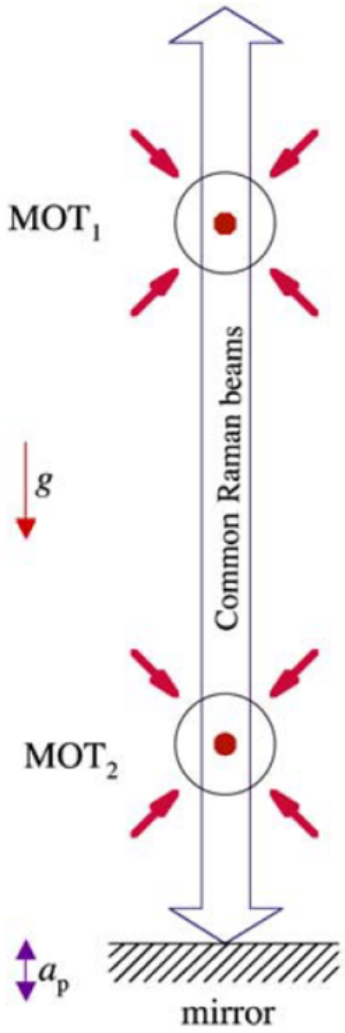

Figure 3.3: Illustration of the QGG Geometry [4]

As shown in figure 3.3, the atom interferometer gravity gradiometer

is composed of two magneto-optic traps (MOTs) which collect and cool up to 10^9 Cesium atoms prior to launching them vertically in a one dimensional atomic fountain. Following launch, both fountains are subjected to a $\pi/2 - \pi - \pi/2$ laser pulse sequence parallel to the vertical launch axis along which the acceleration is to be measured. These pulses, which serve to separate the atoms between hyperfine ground states, redirect and then recombine them, causing a net phase difference $\Delta\phi$ between the two interferometer paths. This phase shift is shown in equation 3.1 to relate directly to the acceleration to which the atomic fountain is subjected.

$$\Delta\phi = k_{eff} \cdot aT^2 \tag{3.1}$$

where

T is the time between pulses

k_{eff} is the effective Raman laser wave number

a is the vector sum of the acceleration due to gravity g and the platform accelerations a_p

The inclusion of platform accelerations in the measurement (which would only be avoidable in an inertial measurement environment) necessitates the use of two MOTs simultaneously with the same Raman laser pulses, as shown in figure 3.3. Differencing the net phase difference from the two MOTs removes the platform accelerations from the equation, allowing for the calculation of a total differential phase shift, shown in equation 3.2, that is related

to the difference between the gravitational accelerations at the locations of the two MOTs. This in line differential acceleration, as discussed in section 2.2.3, is the observable desired for the estimation process.

$$\Delta\Phi = \Delta\phi_1 - \Delta\phi_2 = k_{eff}(g_1 - g_2)T^2 \tag{3.2}$$

Several design aspects of the atom interferometer factor in determining the accuracy of the QGG. Most notable are the temperatures to which the MOTs cool the atoms, the distance between the MOTs (or gradiometer arm length) and the time between the Raman laser pulses. The gradiometer built for the experiment described in Yu [4], a cold atom interferometer, cools the atoms to a temperature of approximately 2 μK. At this temperature, given a reasonable interrogation time of 5 seconds and a reasonable arm length of 25 cm (more on these below), a QGG is expected to be limited to a sensitivity of 1 E/rt(Hz). As will be discussed in chapter 4, this sensitivity level is not sufficient to allow the hybrid architecture to improve upon the performance of the GRACE-FO mission. However, gradiometer where the atoms are cooled to the Bose-Einstein Condensate (BEC) state, in the range of 0.1 - 1 nK, would lead to improved sensitivity levels. Given the 5 s interrogation time and 25 cm arm length, the QGG sensitivity would reach of 1 mE/rt(Hz).

This improvement in sensitivity created by cooling the atoms to BEC temperatures, while significant, will still prove insufficient for allowing the hybrid architecture to recover gravity field maps more accurate than those

recovered by GRACE-FO. However, improvements in sensitivity can still be made with larger interrogation times and arm length. Interrogation time directly impacts gradiometer sensitivity due to the presence of its square, T^2, in equation 3.2. By increasing the interrogation time and therefore the magnitude of the total differential phase shift, the same difference between the two gravitational acceleration values causes a shift of greater magnitude in the total differential phase shift, allowing for higher sensitivity to the difference between those two values. The gradiometer arm length, the distance between the two MOTs that create the atomic fountains, impacts the gradiometer sensitivity as it directly determines the difference between the two gravitational acceleration values. An increased distance between the MOTs allows for a greater understanding of the change in gravity along the measurement axis, and therefore a higher level of sensitivity for the QGG. Increasing both the interrogation time and arm length to the greatest possible extent on the satellite - approximately 30 s and 1 m, respectively - should allow for QGG sensitivity to reach levels between 10-100 μE/rt(Hz) [36]. Chapter 4 will provide an assessment of the possible increases in accuracy that sensitivities in this range are sufficient for the hybrid architecture to achieve over the accuracy level of GRACE-FO. Technology currently under development is expected to lead to QGG of further improved sensitivity to the level of 1 μE/rt(Hz) [36].

3.3.2 Signal Size

Viewed through the lens of gravity gradients, the Earth's gravity field is best considered in three separate parts: the central term, the static gravity field due to spherical harmonic terms, and temporal variations. Each of these three components of the Earth's total gravity field create gravity gradient signals at different orders of magnitude. A local gravity gradient tensor at a given location anywhere around the Earth is described in the following form.

$$\overleftrightarrow{G}_{ENU} = \begin{bmatrix} G_{EE} & G_{EN} & G_{EU} \\ G_{EN} & G_{NN} & G_{NU} \\ G_{EU} & G_{NU} & G_{UU} \end{bmatrix} \tag{3.3}$$

This tensor is in the local East-North-Up frame (ENU). The total gradient values in this tensor are of the following orders of magnitude (in units Eotvos, E, where $1E = 10^{-9}\frac{m}{s^2}/m$). It is mainly the terms along the diagonal of this tensor that are of interest. The satellite will be flying in a near-polar orbit; in a perfectly polar orbit, the X, Y and Z axes of the on-board Satellite Reference Frame (SRF), also known in astrodynamics literature as the Local Vertical, Local Horizontal (LVLH) frame, are exactly equivalent to ± N, ± E and -U axes at all times, respectively. As the QGG must be aligned with one of these main three axes, measurements must be collected along one of the main three local axes.

$$
\begin{aligned}
G_{EE}, G_{NN}, G_{UU} &\approx O(10^3) \\
G_{NU} &\approx O(10^0) \\
G_{EN}, G_{EU} &\approx O(10^{-3})
\end{aligned}
\tag{3.4}
$$

$$
\begin{aligned}
U_{EE} =& \frac{1}{r^2 \cos^2\phi} U_{\lambda\lambda} - \frac{\tan\phi}{r^2} U_{\phi} + \frac{1}{r} U_r \\
U_{EN} =& \frac{1}{r^2 \cos\phi} U_{\lambda\phi} + \frac{\sin\phi}{r^2 \cos^2\phi} U_{\lambda} \\
U_{EU} =& \frac{1}{r \cos\phi} U_{\lambda r} - \frac{1}{r^2 \cos\phi} U_{\lambda} \\
U_{NN} =& \frac{1}{r} U_{\phi\phi} + \frac{1}{r} U_r \\
U_{NU} =& \frac{1}{r} U_{\phi r} - \frac{1}{r^2} U_{\phi} \\
U_{UU} =& U_{rr}
\end{aligned}
\tag{3.5}
$$

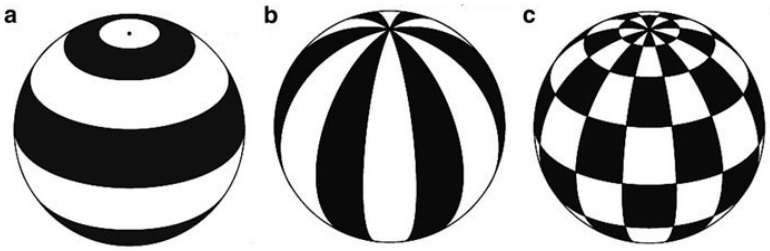

Figure 3.4: Visual Representation of (a) Zonal, (b) Sectoral and (c) Tesseral Spherical Harmonic Values

Due to the forms of the directional second derivatives of the Earth's potential, as described by Bettadpur, Schutz and Lundberg [37], and shown in equation 3.5, the G_{EN} and G_{EU} terms have no dependence upon the zonal harmonic terms (including J_2). All terms in the equations for these two components have at least one derivative taken with respect to the longitude. As zonal

terms are axially symmetric around the globe, shown in figure 3.4, longitudinal derivatives necessarily exclude their effect. Therefore, while the magnitude G_{NU} is scaled with respect to the point mass (and therefore the diagonal gravity gradient terms) by the size of the largest zonal term, $J_2 \approx O(10^{-3})$, the magnitudes of G_{EN} and G_{EU} are scaled with respect to the point mass by the size of the largest non-zonal harmonic term, $\approx O(10^{-6})$. This results in the orders of magnitude listed in equation 3.4.

The total diagonal gravity gradient signals collected throughout a day are shown below. Note that variations on this scale are due to spatial movement of the satellite throughout the gravity field, not time.

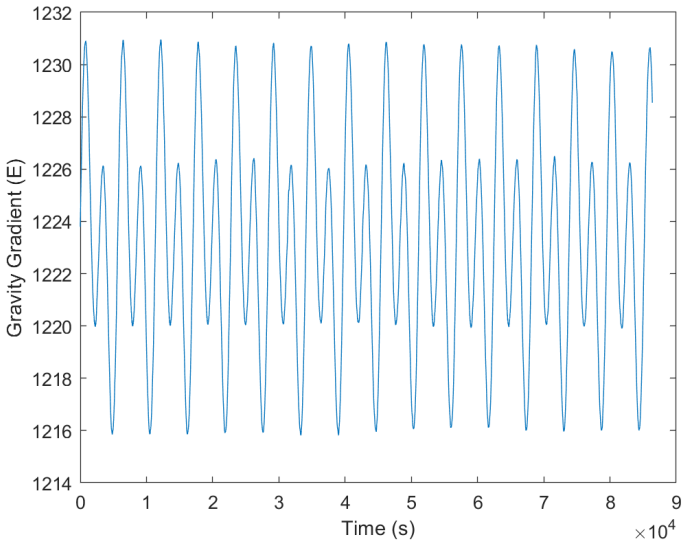

Figure 3.5: Total EE Gravity Gradient Signal through One Day

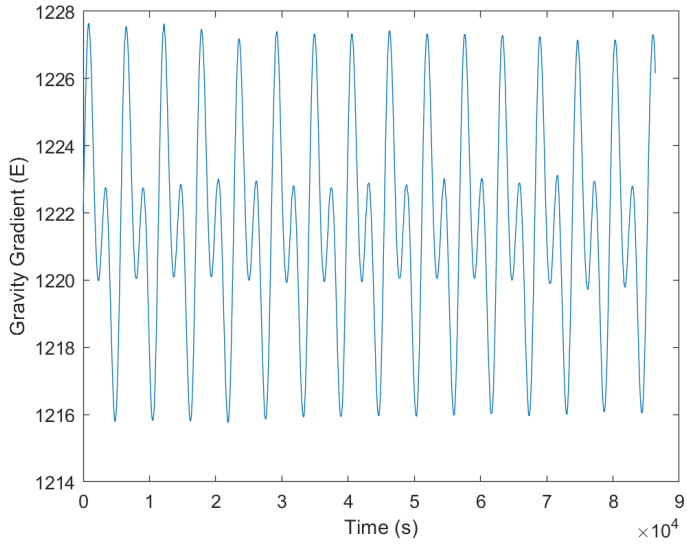

Figure 3.6: Total NN Gravity Gradient Signal through One Day

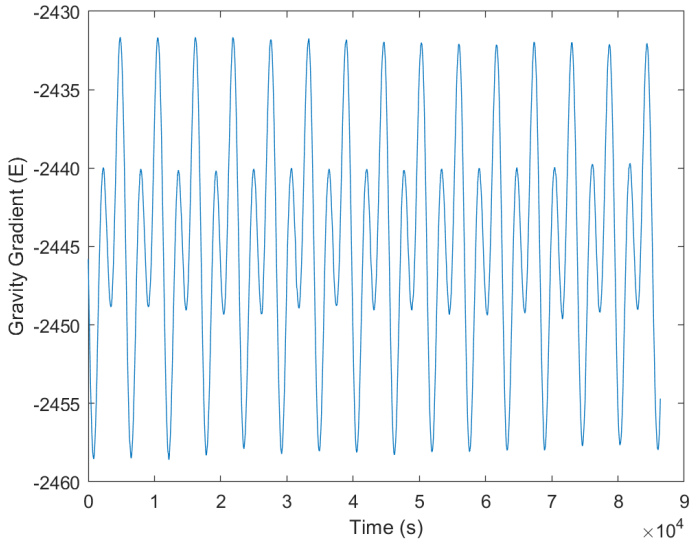

Figure 3.7: Total UU Gravity Gradient Signal through One Day

These total signals are dominated by the central term. At all points on the surface of the Earth, the diagonal central gravity gradient signals are approximately equal to the following, units again E.

$$\overleftrightarrow{G}_{central} = \begin{bmatrix} -1200 & \dots & \dots \\ \dots & -1200 & \dots \\ \dots & \dots & 2400 \end{bmatrix} \tag{3.6}$$

Removing the signal from the two body term, with gradients of order of magnitude $O(10^3)$ E, allows for a clear picture of the static gravity field due to the spherical harmonic terms. The diagonal terms of this portion of the gravity field are of order of magnitude $O(10^0)$ E. This is well represented by table 3.1, which displays the RMS of gravity gradient signals collected in simulation throughout a day following the removal of the signal due to the two body term. Once again, note that fluctuations are spatial, not temporal; as the name suggests, this portion of the gravity field is constant with respect to time.

Table 3.1: Static Gravity Field Signal Spatial RMS, Collected in Simulation at 500 km Altitude

Gravity Gradient Term	RMS (E)
GG_{EE}	3.01
GG_{EN}	0.03
GG_{EU}	0.09
GG_{NN}	4.22
GG_{NU}	4.83
GG_{UU}	7.23

Note the difference between the NU term and the other off-diagonal terms, for reasons noted above. This will be especially relevant to section 3.4.

As with the central term, fluctuations in the signal in the radial direction (UU) are approximately twice the size of the fluctuations in the fluctuations in the other diagonal directions; this will hold true for the time variable signal as well. For purposes of seeing the largest signal, figures 3.8 and 3.9 map the fluctuations of the radial gravity gradient signals from the average gravity field, as calculated at two altitudes. Figure 3.9 shows fluctuations in the static signal as calculated at 450km altitude, similar to the altitude at which the GRACE missions (and a potential future hybrid mission) orbit. Figure 3.8 shows fluctuations in the static signal as calculated at 260km altitude.

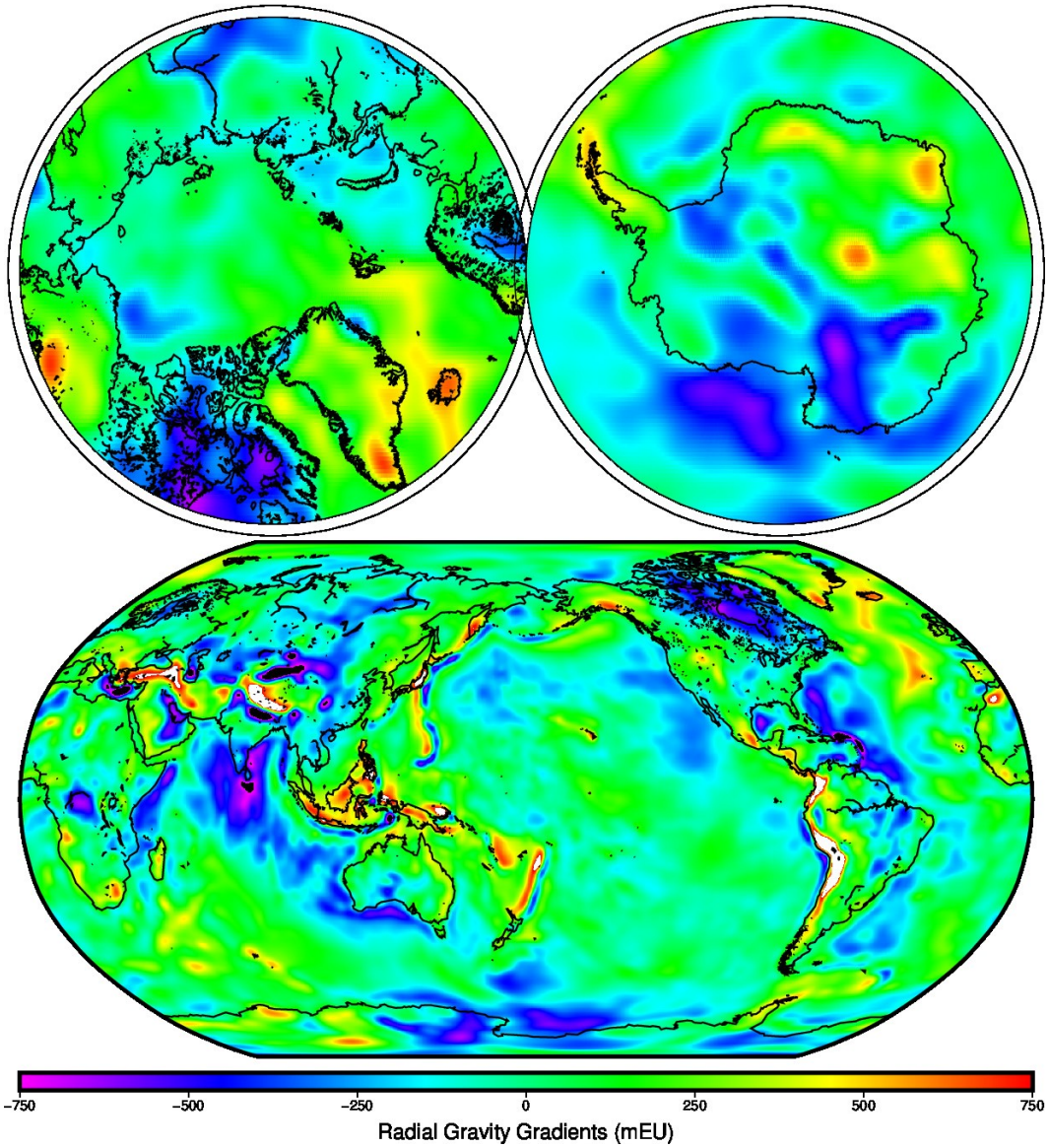

Figure 3.8: Radial Static Spherical Harmonic Gravity Gradients Spatial Fluctuations at 260km Altitude

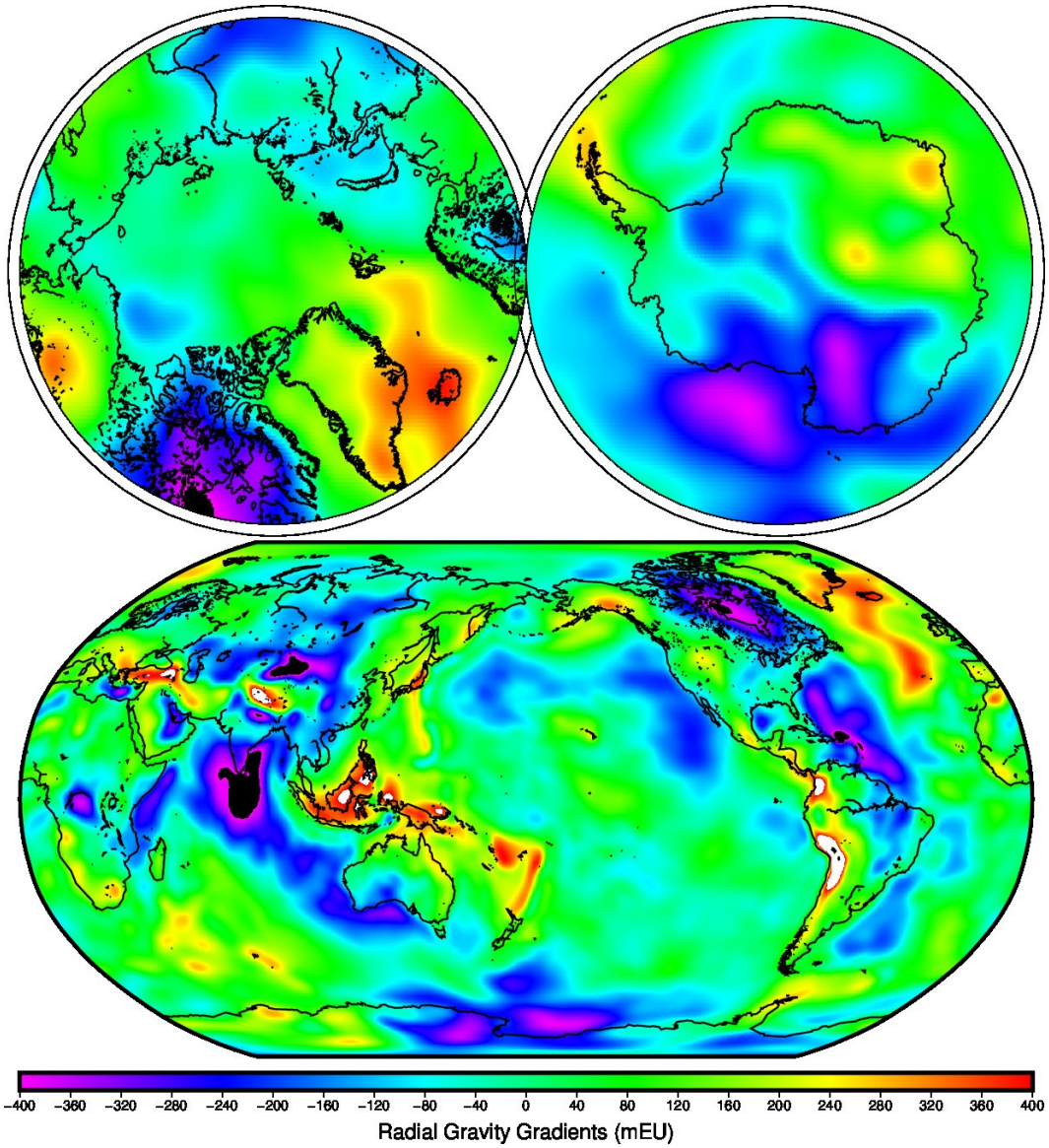

Figure 3.9: Radial Static Spherical Harmonic Gravity Gradients Spatial Fluctuations at 450km Altitude

The signal collected at the higher altitude is smaller in magnitude and

contains far less detail about the subtleties of the gravity field, particularly evident around Indonesia and Malaysia, in the regions of the Pacific south of Japan and north of New Zealand and off the west coast of South America. This higher altitude is necessary for the missions to remain in orbit for an extended period of time, but it comes at the cost of this detail.

Removing the signal due to the static gravity fields reveals the signal due to time variations in the gravity field, the intended observable of the QGG on the hybrid architecture. Similar to the signal due to the static gravity field, the time variations are best described as fluctuations from the average. Images 3.10, 3.11 and 3.12 display these fluctuations as corrections to the prior based knowledge gravity field based upon data collected by GRACE-FO at 450km altitude and averaged over a month. These corrections represent signals that were previously unknown or unmodeled. The months chosen for display show that, while the signal at various points across the surface of the Earth is dependent upon the time of year, the maximum magnitude of the fluctuations is always approximately $100\mu E$.

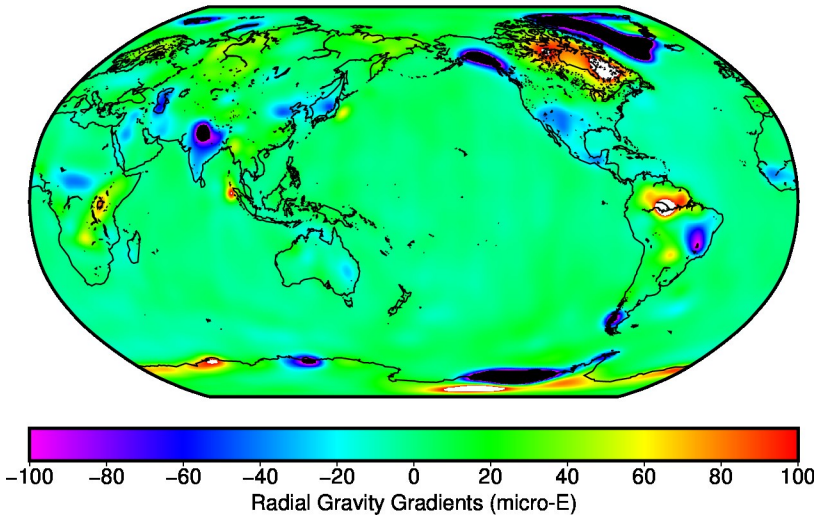

Figure 3.10: June 2018 Radial Gravity Gradients Due to the GRACE-FO Monthly Average Estimates

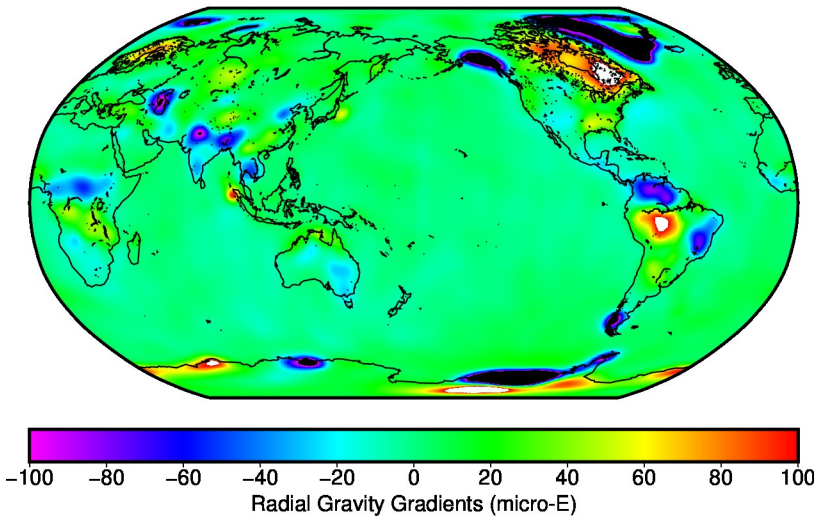

Figure 3.11: February 2019 Radial Gravity Gradients Due to the GRACE-FO Monthly Average Estimates

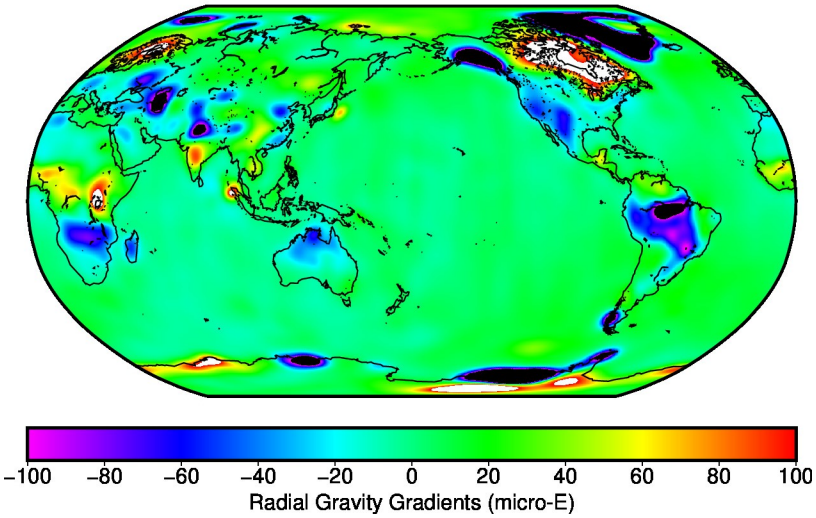

Figure 3.12: November 2020 Radial Gravity Gradients Due to the GRACE-FO Monthly Average Estimates

Once again, the GG_{EE} and GG_{NN} signals vary at approximately half the magnitude of the GG_{UU} signal. The diagonal elements of the time varying gravity gradient signal can therefore be expected to have the following orders of magnitude.

$$\begin{aligned} G_{UU,tv} &\approx O(10^{-4}) \\ G_{EE,tv}, G_{NN,tv} &\approx O(10^{-5}) \end{aligned} \tag{3.7}$$

3.4 Pointing Error Realization

The hybrid architecture is designed to measure gravity gradients across the lead satellite in the SRF. The SRF is defined with the X-axis in the positive In-track direction, the Y-axis in the positive Cross-track direction and the Z-

axis in the negative Radial direction. The single-axis QGG will point in the Cross-track (Y) direction on the satellite; this section will serve to justify this choice as the best for reaching the highest possible level of pointing knowledge, and therefore the best for the highest possible level of accuracy in time variable gravity gradient collection.

Gravity gradient tensors are understood in the ENU frame, as described in equation 3.3, with orders of magnitude as listed in equation 3.4. An analysis of the rotation between ENU and SRF is therefore relevant to understanding the error propagation in rotating from between frames.

The rotation from ENU to SRF, described in equation 3.8, can be represented by a [3,2,1] rotation. The full rotation matrix, M, is given by equation 3.9, where M_3 is a rotation about the Z-axis, M_2 is a rotation about the Y-axis and M_1 is a rotation about the X-axis. These three rotations in combination produces the full rotation matrix, M.

$$\begin{aligned} M &= M_1(\psi)M_2(\theta)M_3(\phi) \\ \vec{r}_{SRF} &= M\vec{r}_{ENU} \\ \overleftrightarrow{G}_{GRF} &= M\overleftrightarrow{G}_{ENU}M^T \end{aligned} \tag{3.8}$$

$$M = \begin{bmatrix} \cos\phi\cos\theta & \sin\phi\cos\theta & -\sin\theta \\ \cos\phi\sin\theta\sin\psi - \sin\phi\cos\psi & \sin\phi\sin\theta\sin\psi + \cos\phi\cos\psi & \cos\theta\sin\psi \\ \cos\phi\sin\theta\cos\psi + \sin\phi\sin\psi & \sin\phi\sin\theta\cos\psi - \cos\phi\sin\psi & \cos\theta\cos\psi \end{bmatrix} \tag{3.9}$$

The angles used to rotate the in-flight measurement of the gravity gradients between these two frames can be expected to have some amount of error accompanying them. This results from error in the knowledge (dependent upon the attitude sensors on the satellite) of the rotation angles between the frames. The full rotation angles can be represented by the following equations.

$$\begin{aligned} \psi &= \bar{\psi} + \epsilon_\psi \\ \theta &= \bar{\theta} + \epsilon_\theta \\ \phi &= \bar{\phi} + \epsilon_\phi \end{aligned} \tag{3.10}$$

For each angle, $\bar{\alpha}$ represents the true value and ϵ represents the error. The following trigonometric identities are useful for expanding the terms in the rotation matrix.

$$\begin{aligned} \sin\bar{\alpha} + \epsilon &= \sin\bar{\alpha}\cos\epsilon + \cos\bar{\alpha}\sin\epsilon \\ \cos\bar{\alpha} + \epsilon &= \cos\bar{\alpha}\cos\epsilon - \sin\bar{\alpha}\sin\epsilon \end{aligned} \tag{3.11}$$

Applying these identities across the rotation matrix M and expanding all terms, the rotation matrix can then be split into the sum of two matrices.

$$M = \bar{M} + \Delta \tag{3.12}$$

$\bar{M}$ is the true rotation between the frames and Δ is the erroneous rotation. $\bar{M}$ has the same form as M, given by equation 3.9, with all of the

angles replaced by the true angle values, $\bar{\alpha}$. Δ takes the form given term by term in equation 3.13, derived through symbolic manipulation in MATLAB™.

$$
\begin{aligned}
\Delta_{1,1} =&\epsilon_\theta\epsilon_\phi \sin\theta \sin\phi - \epsilon_\phi \cos\theta \sin\phi - \epsilon_\theta \sin\theta \cos\phi \\
\Delta_{1,2} =& - \epsilon_\theta\epsilon_\phi \sin\theta \cos\phi + \epsilon_\phi \cos\theta \cos\phi - \epsilon_\theta \sin\theta \sin\phi \\
\Delta_{1,3} =& - \epsilon_\theta \cos\theta \\
\Delta_{2,1} =&\epsilon_\psi\epsilon_\phi \sin\psi \cos\phi + \epsilon_\psi\epsilon_\theta \cos\psi \cos\theta \cos\phi - \epsilon_\psi\epsilon_\phi \cos\psi \sin\theta \sin\phi \\
&- \epsilon_\theta\epsilon_\phi \sin\psi \cos\theta \sin\phi - \epsilon_\psi\epsilon_\theta\epsilon_\phi \cos\psi \cos\theta \sin\phi + \epsilon_\psi \sin\psi \sin\phi \\
&- \epsilon_\phi \cos\psi \cos\phi + \epsilon_\psi \cos\psi \sin\theta \cos\phi + \epsilon_\theta \sin\psi \cos\theta \cos\phi \\
&- \epsilon_\phi \sin\psi \sin\theta \sin\phi \\
\Delta_{2,2} =&\epsilon_\psi\epsilon_\phi \sin\psi \sin\phi + \epsilon_\psi\epsilon_\theta \cos\psi \cos\theta \sin\phi + \epsilon_\psi\epsilon_\phi \cos\psi \sin\theta \cos\phi \\
&+ \epsilon_\theta\epsilon_\phi \sin\psi \cos\theta \cos\phi + \epsilon_\psi\epsilon_\theta\epsilon_\phi \cos\psi \cos\theta \cos\phi - \epsilon_\phi \cos\psi \sin\phi \\
&- \epsilon_\psi \sin\psi \cos\phi + \epsilon_\psi \cos\psi \sin\theta \sin\psi + \epsilon_\theta \sin\psi \cos\theta \sin\phi \\
&+ \epsilon_\phi \sin\psi \sin\theta \cos\phi \qquad (3.13) \\
\Delta_{2,3} =& - \epsilon_\psi\epsilon_\theta \cos\psi \sin\theta + \epsilon_\psi \cos\psi \cos\theta - \epsilon_\theta \sin\psi \sin\theta \\
\Delta_{3,1} =&\epsilon_\psi\epsilon_\phi \cos\psi \cos\phi - \epsilon_\psi\epsilon_\theta \sin\psi \cos\theta \cos\phi - \epsilon_\theta\epsilon_\phi \cos\psi \cos\theta \sin\phi \\
&+ \epsilon_\psi\epsilon_\phi \sin\psi \sin\theta \sin\phi + \epsilon_\psi\epsilon_\theta\epsilon_\phi \sin\psi \cos\theta \sin\phi + \epsilon_\psi \cos\psi \sin\phi \\
&+ \epsilon_\phi \sin\psi \cos\phi + \epsilon_\theta \cos\psi \cos\theta \cos\phi - \epsilon_\psi \sin\psi \sin\theta \cos\phi \\
&- \epsilon_\phi \cos\psi \sin\theta \sin\phi \\
\Delta_{3,2} =&\epsilon_\psi\epsilon_\phi \cos\psi \sin\phi + \epsilon_\theta\epsilon_\phi \cos\psi \cos\theta \cos\phi - \epsilon_\psi\epsilon_\theta \sin\psi \cos\theta \sin\phi \\
&- \epsilon_\psi\epsilon_\phi \sin\psi \sin\theta \cos\phi - \epsilon_\psi\epsilon_\theta\epsilon_\phi \sin\psi \cos\theta \cos\phi + \epsilon_\phi \sin\psi \sin\phi \\
&- \epsilon_\psi \cos\psi \cos\phi + \epsilon_\theta \cos\psi \cos\theta \sin\phi + \epsilon_\phi \cos\psi \sin\theta \cos\phi \\
&- \epsilon_\psi \sin\psi \sin\theta \sin\phi \\
\Delta_{3,3} =&\epsilon_\psi\epsilon_\theta \sin\psi \sin\theta - \epsilon_\psi \sin\psi \cos\theta - \epsilon_\theta \cos\psi \sin\theta
\end{aligned}
$$

Substituting the expanded rotation matrix from equation 3.12 into the dyad rotation from the third line of equation 3.8, the rotation can be expanded; the first term in 3.14 is the true rotation; the full rotation error can therefore be represented by equation 3.15.

$$\overleftrightarrow{G}_{SRF} = \bar{M}\overleftrightarrow{G}_{ENU}\bar{M}^T + \bar{M}\overleftrightarrow{G}_{ENU}\Delta^T + \Delta\overleftrightarrow{G}_{ENU}\bar{M}^T + \Delta\overleftrightarrow{G}_{ENU}\Delta^T \quad (3.14)$$

$$E_{\overleftrightarrow{G}_{SRF}} = \bar{M}\overleftrightarrow{G}_{ENU}\Delta^T + \Delta\overleftrightarrow{G}_{ENU}\bar{M}^T + \Delta\overleftrightarrow{G}_{ENU}\Delta^T \quad (3.15)$$

Simulations performed for this study have the hybrid architecture in the same near-polar orbit GRACE-FO utilizes. Taking this orbit to be perfectly polar for simplicity, the angles to rotate from ENU to SRF are $\psi = 0$, $\theta = \pi$ and $\phi = \frac{\pi}{2}$. The true rotation matrix takes the following values.

$$\bar{M} = \begin{bmatrix} 0 & 1 & 0 \\ 1 & 0 & 0 \\ 0 & 0 & -1 \end{bmatrix} \quad (3.16)$$

This means, as mentioned in section 3.3.2, the following axes are equivalent: $X_{SRF} = N_{ENU}$, $Y_{SRF} = E_{ENU}$ and $Z_{SRF} = -U_{ENU}$ (when the satellite is ascending; the signs change in the X_{SRF} and Y_{SRF} equivalencies when the satellite is descending). Rotating the ENU gravity gradient dyad through the true angles, the diagonal SRF gradient terms are given by equation 3.17.

$$
\begin{aligned}
GG_{XX} &= GG_{NN} \\
GG_{YY} &= GG_{EE} \\
GG_{ZZ} &= GG_{UU}
\end{aligned}
\tag{3.17}
$$

However, including the error, each diagonal SRF gradient can be expressed as six separate terms, one for each of the ENU gradient values. For visual simplicity, these terms are listed in table 3.2. All cubic or higher order error terms are discarded as small enough to be negligible.

Table 3.2: SRF Gravity Gradients Expression by ENU Terms

	GG_{XX}	GG_{YY}	GG_{ZZ}
GG_{EE}	ϵ_ϕ^2	1	ϵ_ψ^2
GG_{EN}	$-2\epsilon_\phi^2$	$2\epsilon_\phi + 2\epsilon_\psi\epsilon_\theta$	$-2\epsilon_\psi\epsilon_\theta$
GG_{EU}	$2\epsilon_\theta\epsilon_\phi$	$2\epsilon_\psi$	$-2\epsilon_\psi - 2\epsilon_\theta\epsilon_\phi$
GG_{NN}	1	ϵ_ϕ^2	ϵ_θ^2
GG_{NU}	$-2\epsilon_\theta$	$2\epsilon_\psi\epsilon_\phi$	$2\epsilon_\theta - 2\epsilon_\psi\epsilon_\phi$
GG_{UU}	ϵ_θ^2	ϵ_ψ^2	1

Each SRF gravity gradient is equal to the sum of the column under it, with each value multiplied by the ENU gradient term at the row head. These are again derived through symbolic manipulation in MATLAB™.

The error in each rotation angle is taken to be approximately 1 μRad ($\approx O(10^{-6})$), the error expected from the attitude sensors utilized by the IceSAT-2 mission, one of the most advanced currently available [38]. Utilizing this error size and the orders of magnitude of the total ENU gravity gradient values listed in equation 3.4, the order of magnitudes of the largest, and therefore overall,

errors accompanying each of the diagonal SRF gravity gradient values are calculated. For example, the XX gradient's largest error comes from the GG_{NU} term - the true gradient value is $O(10^0)$ and it is multiplied by a single rotation error, introducing a gradient error that is $O(10^{-6})$. This is larger than the error introduced by, for example, the GG_{UU} term, which has a larger true value with $O(10^3)$ but is multiplied by the square of a rotation error, introducing a gradient error that is $O(10^{-9})$. The same calculations are performed with all terms in table 3.2, with the following being the orders of magnitude of the largest error introduced along each SRF axis.

$$\begin{aligned} E_{GG_{XX}} &\approx O(10^{-6}) \\ E_{GG_{YY}} &\approx O(10^{-8}) \\ E_{GG_{ZZ}} &\approx O(10^{-6}) \end{aligned} \tag{3.18}$$

Comparing these error magnitudes with the time variable signal magnitudes listed in equation 3.7, it is evident GG_{EE} is the best option for data collection. The signal along this axis is three orders of magnitude larger than the noise expected, given pointing knowledge error of magnitude $O(10^{-6})$ radians. The GG_{UU} signal is only two orders larger than the associated noise, and the GG_{NN} signal only 1 order larger than the associated noise. Due to this best signal to noise ratio, the EE gravity gradient value will provide the most information for contribution to the estimation of gravity fields.

3.5 Aliasing Error Realization

As described in P.F. Thompson's dissertation [15], aliasing error in gravity sensing is the result of differences between the Earth's true gravity field and the nominal model utilized in preparing partials for estimation from collected observations. Certain time-variable aspects of the Earth's gravity field, particularly short-period effects, are not captured by current models to a high degree of accuracy. Gravity fields recovered from observations through the process described in section 2.3 thus contain error not only due to the limitations of the instruments on the satellites, but also due to incorrect aspects of the nominal field that must be used in the process of estimating the true gravity field.

A separate set of simulations are conducted to model the effect of aliasing error on the hybrid QGG-SST architecture. In this set of simulations, following the creation of observations and the addition of measurement and instrument noise, partials are generated for the data with respect to orbits integrated using a different gravity field than the truth field used to generate the observations. For the construction of this other field (referred to herein as the nominal field) the same base static gravity field - GIF48.2000.GEO - is utilized. However, different models are included for various elements that cause short-period variations in the gravity field, leading to slight differences between the nominal and truth gravity models - making the nominal field incorrect within the universe of the simulation.

The true and nominal gravity field models in the simulation are de-

scribed in the following equation.

$$\begin{aligned} G_{true}(t) &= G + \delta G_{true}(t) \\ G_{nom}(t) &= G + \delta G_{nom}(t) \end{aligned} \tag{3.19}$$

where

G is the static gravity field

$\delta G_i(t)$ represents perturbations due to time-variable potential

Through the least squares estimation process, an update to the nominal gravity model is found such that measurement residuals are minimized. This update is in the form of a set of constant corrections to each spherical harmonic coefficient during the data span T_s. Effectively, the update the information contributed by the simulated mission; it is represented below.

$$\delta\hat{G}(T_s) = L\{Y_i - f(G_{nom}(t_i)\},\ i = 1, \ldots m \tag{3.20}$$

where

$\delta\hat{G}(T_s)$ is the estimation update over the time span T_s

L is the linearized least squares problem

$Y_i - f(G_{nom}(t_i))$ is the observed minus computed, $O - C$, values

With real mission data, this update would include both desired information about unmodeled phenomena causing temporal variations in geopotential, such as hydrometeorology and ocean dynamics, and the time average

difference between the Earth's true gravity field and the nominal field. In simulations, as these unmodeled phenomena do not exist in the truth field, the update ideally should only contain the time averaged difference between the two fields. However, this is not the case; error is introduced to the update through measurement noise, inconsistencies between the true and nominal fields and inherent limitations of the estimation process itself [15].

$$\delta\hat{G}(T_s) \approx < G_{true}(t) > - < G_{nom}(t) > \approx < \delta G_{true}(t) > - < \delta G_{nom}(t) > \tag{3.21}$$

The error (which is dominated by aliasing) is then the difference between the two sides of equation 3.21.

$$\epsilon = \delta\hat{G}(T_s) - (< \delta G_{true}(t) > - < \delta G_{nom}(t) >) \tag{3.22}$$

As the exact time average difference between the true and nominal fields can be calculated in the simulation, this difference can be removed from the update. This permits direct calculation of aliasing error, ϵ, in equation 3.22. An understanding of the exact impact aliasing error has upon the hybrid architecture during simulations will allow for more precise removal of this error source while processing real data from a mission utilizing this architecture.

Chapter 4

Configuration Parametric Study

4.1 Introduction

The simulations performed and analyzed in this chapter model a hybrid gravity sensing architecture that collects both gravity gradient and satellite-to-satellite tracking data, and will serve as a proof of measurement concept for such a mission. The simulated architecture contains all of the instruments from the GRACE-FO mission, which collects SST, and a QGG as developed by Yu et al [4]. The simulation mission design maintains many aspects of the GRACE missions, utilizing a constellation of two satellite in the same 500 km radius near-polar orbit, separated by 220 $\pm$ 50 km [25, 1]. The simulation procedure applies white noise to several types of instrument data in place of real-life instrument error. The noise levels applied in simulations of the GRACE-FO for the accelerometer and SST are maintained throughout all simulations. The accelerometer full-scale range applied is $5 \times 10^{-5} \frac{m}{s^2}$ and the SST PSD is 0.08 $\mu m \sqrt{Hz}$, as described in section 3.2.

As shown through analysis in section 3.4, the SRF Y axis (equivalent to the orbital cross-track axis) is the optimal pointing direction for the QGG, minimizing contributions from error in pointing knowledge. This chapter, prior

to discussion of full simulations, will review simulated gravity gradient data collected along all three SRF axes to demonstrate the validity of this analysis. This review will be performed with and without the application of noise in the numerical simulations to the star camera (SCA) data, which, as the main attitude determination instrument on board, contributes significantly to the satellite's pointing knowledge. SCA will serve in this study as a stand in for a general attitude determination system.

The star camera instrument on each satellite simulated herein consists of two separate star camera sensor heads, each of which collects and outputs attitude data every five seconds. Noise is simulated and applied by first rotating the true orientation to the frame of each star camera sensor head, then corrupting that orientation data according to the PSD of the measurement model applied. The information from each of the star cameras is then optimally combined. Quaternion data and measurement noise from each sensor head is rotated into the SRF, and the difference between the attitude orientations reported by each are calculated as small angle values. This difference is mapped to an optimal change from one of the sensor heads to represent the rotation from the inertial frame to the SRF.

The necessity of a hybrid architecture that incorporates SST, QGG and GPS data will be shown via the overall contribution of each data type to the simulation results. It is shown through simulations that a mission utilizing only QGG and GPS data will not be capable of outperforming GRACE-FO at the simulation altitude of 450 km, as a crucial amount of information that would be

gathered by the SST measurements goes uncollected by such an architecture. It becomes evident that the QGG and SST measurements complement each other; each is able to make unique contributions to the estimation of certain spherical harmonic coefficients the other does not.

The simulations will be used to evaluate the performance of the hybrid architecture subject to the three error types determined to be most likely to limit its performance: QGG instrument error, pointing knowledge error and aliasing error. SCA is used as the representation of pointing knowledge error in these simulations. As with the other measurement noise types, QGG and SCA error will be modeled with white noise. The architecture will be simulated at varying levels of each of these error types. The primary metric for evaluation of the results from these simulations will be degree difference variance (DDV). DDV is a measure of how similar the gravity field resulting from the estimation process is to the true gravity field used to generate the observation data. A gravity field recovered by the estimation process is shown to be more similar to the simulation's true gravity field with smaller DDV values.

$$DDV_l = a\sqrt{\sum_{m=0}^{l}(C_{lm}^{est} - C_{lm}^{true})^2 + (S_{lm}^{est} - S_{lm}^{true})^2} \tag{4.1}$$

where

a is the average radius of the earth, 6378.136×10^6 mm

l and m are the spherical harmonic degree and order, respectively

C_{lm}^{est} and S_{lm}^{est} are the estimated gravity field spherical harmonic values

C_{lm}^{true} and S_{lm}^{true} are the true gravity field spherical harmonic components

Equation 4.1 describes DDV calculated with one cumulative value at each spherical harmonic degree. Results will be given in this manner as well as values at each individual degree and order combination, calculated via a similar equation without the summation.

$$DDV_{lm} = C_{lm}^{est} - C_{lm}^{true} \tag{4.2}$$

The same is done for S coefficients. Results in this study are produced out to degree and order 120. Scaling by the radius of the Earth attains the geoid height error, which represents the contribution from terms of that degree to the total global root mean square geoid error.

The models utilized for simulations investigating aliasing error are discussed. The results of these simulations are evaluated through both DDV and the applicability of resulting gravity fields to smoothing, with the use of gravity field maps for interpretation. As the hybrid architecture is expected to bring about improvements specifically at small spatial scales, specific attention will be given to the results at medium and high degree spherical harmonic values - above degree 20. These values correlate directly with medium and small spatial scales.

4.2 Design of Parametric Study

The simulated orbits are set at the start of each day, or arc, of the simulation with the initial conditions the GRACE satellites had in August of 2008. This orbit is nearly polar, nearly circular and has an altitude of approximately 450 km. There are three types of parameters solved for: local, common and global. Local parameters, such as SST biases, are estimated using only one type of data from one arc. Common parameters, such as accelerometer biases, are estimated using all data types from one arc. Global parameters, such as the spherical harmonic coefficients, are estimated using all data types from all arcs. Implementation of these varying parameter types is discussed in further detail by Gunter [31].

4.2.1 Gradiometer and Pointing Knowledge Error Parameters

Given that that pointing knowledge maintains a high level of importance to the mission specifically because it directly impacts the accuracy of the gradiometer measurements, this error source and the gradiometer error itself are studied in tandem. Each of these sources of error are adjusted to varying levels to establish an idea of how the architecture would perform with different combinations of error from these two sources. The error levels tested for each of these sources are based upon currently achievable and experimental/under development levels of accuracy. The results of these simulations will be compared to both each other and a simulated GRACE-FO mission: a simulation which maintains all of the parameters (including the pointing knowledge) of

GRACE-FO and does not utilize QGG data.

Pointing knowledge error is adjusted in these simulations via the SCA noise levels, but pointing knowledge need not necessarily come from star cameras. Any type of attitude determination system can substitute; star cameras are simply the tools used by the GRACE missions. These star cameras do not carry the same accuracy along each of their three axes, though the order of magnitude along all three axes is the same. For this reason, pointing knowledge error levels will be described by orders of magnitude, rather than exact numbers. The noise levels employed by this study, as described by PSDs, are listed in table 4.1.

Table 4.1: Pointing Knowledge Error Sqare-Root Power Spectral Densities

PSD ($\mu Rad/\sqrt{Hz}$)	Source
O(10)	GRACE-FO Attitude Sensors
O(1)	IceSAT-2 Attitude Sensors [38]
O(0.1)	IRASSI Attitude Determination Estimator [39]

QGG noise at current technology levels, as mentioned in section 3.3.1, can be expected to have a PSD in the range of 10-100 μE/rt(Hz), with technology currently under development expected to yield noise levels as low as 1 μE/rt(Hz) [36]. These three noise levels - 1, 10 and 100 μE/rt(Hz) - will be utilized by this study. In following from section 3.3.2, the GG_{EE} component at altitude 450 km of the time variable gravity gradient signal is unlikely to ever reach a magnitude of 100μE. The expectation is that the simulations limited

by instrument noise (in which aliasing error is not applied) with a QGG noise PSD of 100μE will provide no significant improvements over the GRACE-FO mission. However, it is expected that with PSDs of 1μE and 10μE, the QGG instrument will be able to collect meaningful data that will contribute to large improvements over GRACE-FO.

4.2.2 Aliasing Study Modeling

As discussed in section 3.5, when creating simulations to study aliasing error, the true gravity field model is different from the nominal gravity field model, which is used to integrate orbits and create partials for estimation from the noisy observation data. This mimics the mission reality that the gravity field based on the best available knowledge at the time will not be a true representation of the Earth's gravity field, particularly not short-period time variable aspects. This introduces aliasing errors to the update, which result from the limited ability of the estimation process to reconcile the results of these short period variations in the observation data due to the inadequacies of the nominal field it is based upon.

The true and nominal fields are each synthesized from a variety of models. These models represent different aspects of the geopotential. For the static field component, both the true and nominal field use the GIF48.2000.GEO model. They use identical static gravity fields because the linearized least-squares process is designed to provide a correction exactly equal to the difference between the true and nominal fields, which would tell us nothing new

with regards to the static fields in these simulations. If a different estimator were used for the simulations or the focus were on the effects of the omission of higher degree terms, the two models would been created using different static gravity fields.

It is in the models used for various sources of time variable gravity that the true and nominal fields in the simulation differ. The models used to construct both the true and nominal gravity field models in simulations for this study are listed in table 4.2.

Table 4.2: Time Variable Gravity Models in True and Nominal Aliasing Simulations

	True	Nominal
Ocean Tides	GOT4.8 [40]	FES2004 [41]
Atmosphere and Non-Tidal Variability in the Oceans	AOD1B RL05 [42]	IB-NCEP [43]
Ocean Pole Tide Model	Desai [44]	Desai
Other Variability Over Land and Ice-Sheets	XBL [45]	None

Model lists are as provided via private communication from Srinivas Bettadpur [46] with descriptions accumulated in the GRACE CSR Level 2 Processing Standards Document [47]

XBL was constructed with a blend of information from GRACE and land surface model data. This includes long period (annual, semi-annual and secular) signals from GRACE and the GLDAS-1 model for high-frequency temporal signals [48]. The process by which these were blended is described

by Sakumura [45]. The true gravity model time average described in equation 3.21 for the aliasing simulations discussed in this chapter will be equal to the mean of the sum of models in the first column.

4.3 Outcomes and Analysis

4.3.1 Validation of Gradiometer Axis for Pointing Knowledge Optimization

Through manipulation of the rotation between the SRF and ENU frames in section 3.4, it was shown that the signal-to-noise ratio for gravity gradient data is largest along the SRF Y axis, equivalent to the ENU E axis. It was determined for this reason that the QGG instrument on the hybrid architecture should collect data along this axis. Prior to analyzing gravity field results from the simulations, this section will analyze the simulated gravity gradient data to validate this conclusion.

The PSDs of the error present, the differences between the O and C values, in gravity gradient data collected along each of the satellite's three axes, calculated in the manner described by Widner [49], are displayed in figures 4.1, 4.2 and 4.3.

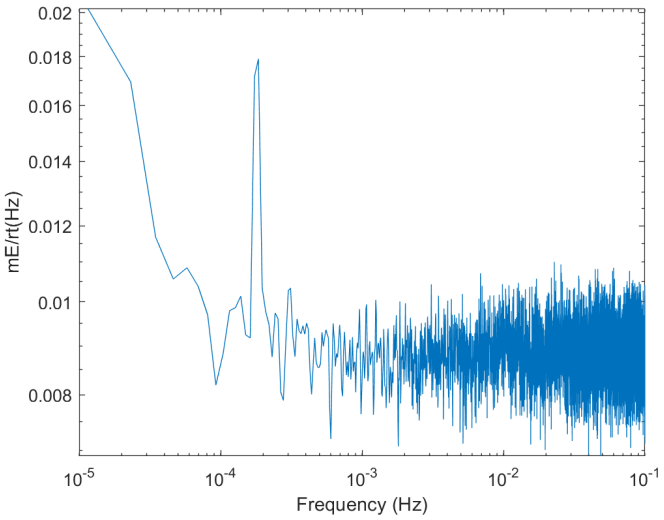

Figure 4.1: Smoothed Power Spectral Density of Monthly Average Gravity Gradient Error along SRF X Axis

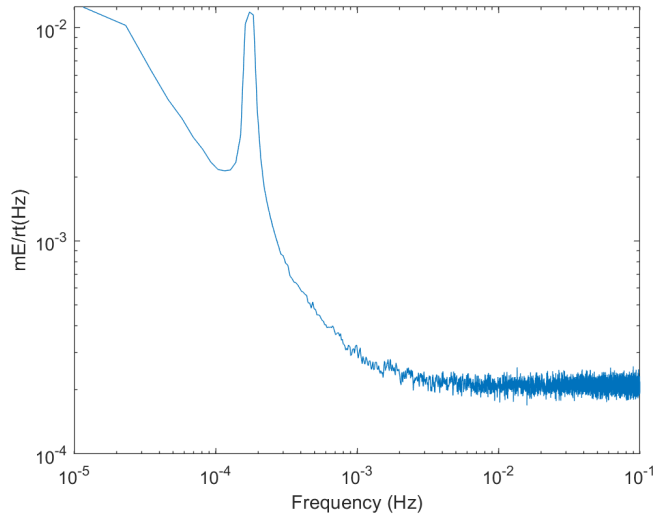

Figure 4.2: Smoothed Power Spectral Density of Monthly Average Gravity Gradient Error along SRF Y Axis

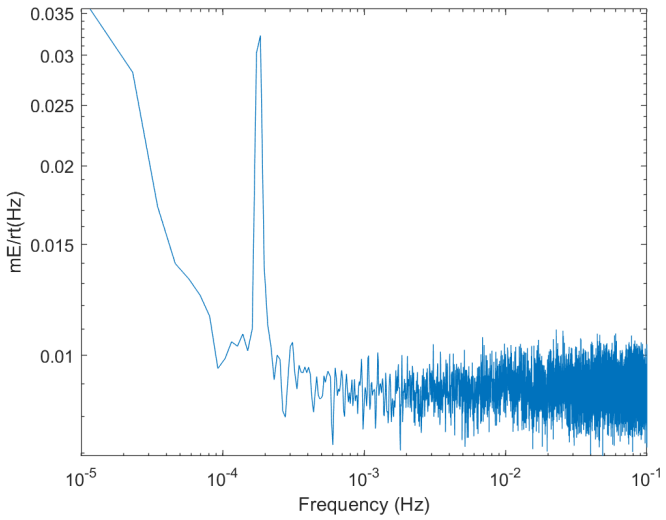

Figure 4.3: Smoothed Power Spectral Density of Monthly Average Gravity Gradient Error along SRF Z Axis

These PSDs are calculated with errors averaged over a full month of simulated data collected. As the majority of X and Z terms are between 0.02 and 0.008 $mE/rt(Hz)$ while the Y terms are between 10^{-2} and 10^{-4} $mE/rt(Hz)$, it is clear upon inspection that the error along the Y axis is less impactful than the error along the two other axes, as expected. Along all three axes, there is a once per revolution spike due to slight errors in the calculated orbit. Having confirmed this to be the case, the results of full simulations with QGG data collected along the SRF Y axis may be discussed.

4.3.2 Hybrid Architecture Data Contribution

Results contained in this section come from four varying architectures. Those architectures collect and estimate using the following combinations of data types: GPS only, SST+GPS, QGG+GPS, and SST+QGG+GPS. Results from each of these architecture, analyzed individually and in comparison to each other, make evident the benefit of a hybrid architecture that utilizes all three data types to outperform the GRACE-FO mission. All simulations analyzed in this subsection are performed with 1 μRad pointing error. Simulations which include QGG data are performed with 1μE QGG error.

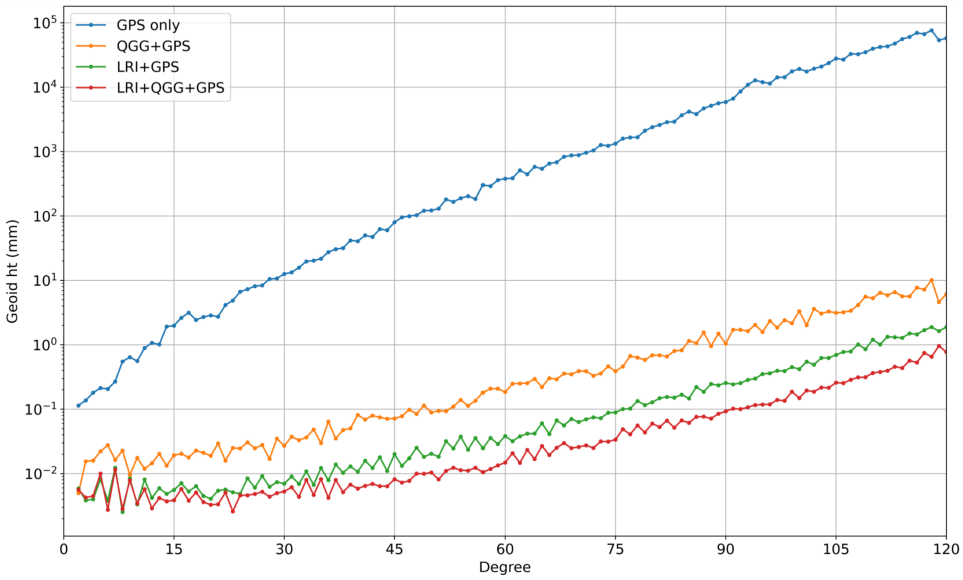

Figure 4.4: All Architecture Type Comparison

Via figure 4.4, it is immediately evident that the GRACE-FO architecture (SST+GPS) performs much better than the QGG+GPS architecture, but

is inferior to the hybrid architecture that uses all three data types, particularly at medium and high degree spherical harmonics. The GPS only solution is vastly inferior to all others.

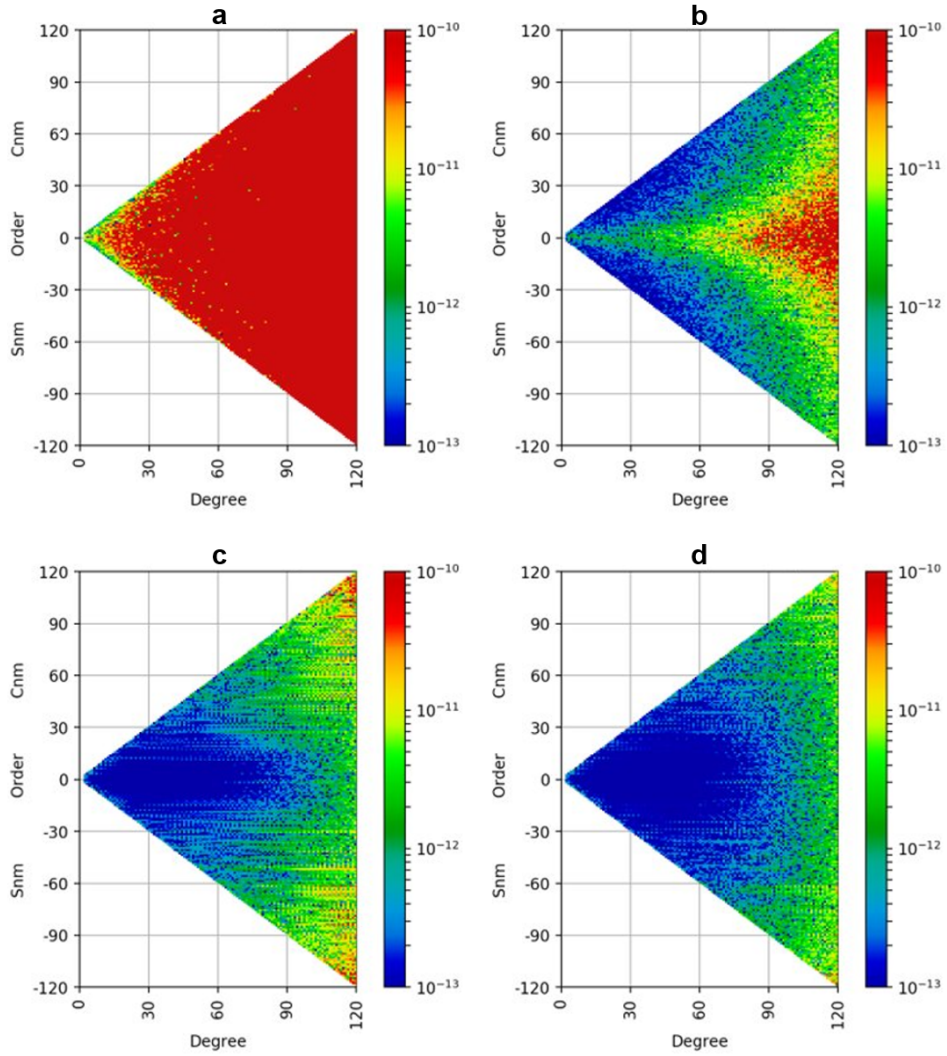

Figure 4.5: All Architecture Type Comparison (Triangle Plots), (a) GPS only, (b) QGG+GPS, (c) SST+GPS and (d) SST+QGG+GPS

The coefficient difference values for each architecture at individual spherical harmonic coefficients in figure 4.5 provide further clarity into the ways the architectures compare with each other. In these plots, blue signifies small DDV - the estimated values are very close to the corresponding true field values, so the noise did not move the estimation far from the truth and these are well determined harmonics. Red signifies large DDV - the estimated values are far from the corresponding true field values, so the noise moved the estimation far from the truth and these harmonics are not as well determined. The QGG+GPS case performs particularly well with sectoral and near-sectoral harmonic values, but fails to provide adequate information for quality estimation of the zonal terms. The SST+GPS case is just the opposite; it performs well with zonal and near-zonal tesseral terms, but fails with all sectoral terms and with near-sectoral tesseral terms higher than degree 50.

The benefits of both of these cases carry into the hybrid architecture. With all three data types, this case recovers zonal terms as well as the SST+GPS case and sectoral terms as well as the QGG+GPS case.

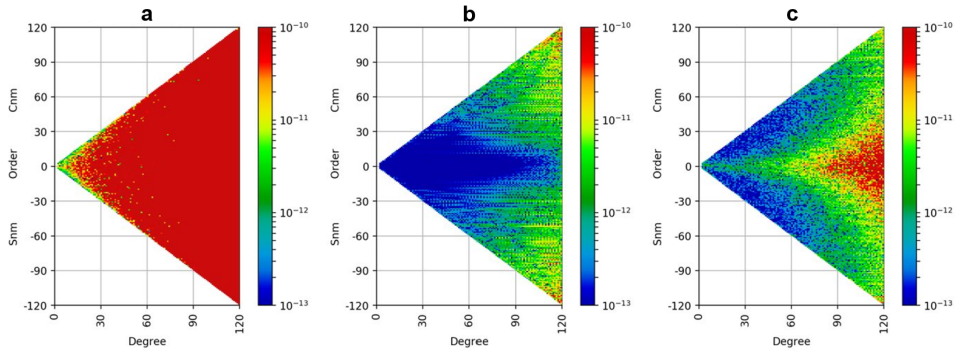

Figure 4.6: Contribution Towards Hybrid Architecture Results from (a) QGG and SST Data Combined, (b) QGG Data andd (c) SST Data

The plots in figure 4.6 show the contribution of each data type to the estimated field of the hybrid architecture. The data contained within these plots is not DDV, but a variation on the DDV. This data is still calculated via the form of equation 4.2, but rather than subtracting the true harmonic coefficient values from the estimated values, it subtracts the estimated coefficient values of one case from the estimated coefficient values of another, as such. Absolute values are shown.

$$DDV_{lm} = C_{lm}^{hyb} - C_{lm}^{contr} \tag{4.3}$$

where

C_{lm}^{hyb} is the spherical harmonic coefficient estimated by the hybrid architecture

C_{lm}^{contr} is the spherical harmonc coefficient estimated by the simulation

using the data types not included in the contribution

This means that, for plot (a), the calculation of the contribution of QGG and SST combined involved subtracting from the hybrid estimation the GPS only estimation, and so on. In this case, blue means the contribution of a data type is low at that harmonic value, while red shows a high contribution.

This data confirms the conclusions drawn from 4.5. The QGG data makes the greatest contributions at the sectoral and near-sectoral tesseral values, while the SST data makes the greatest contributions at zonal and near-zonal tesseral terms. These results also confirm those collected by Yi and Rummel; in a gravity field recovered with SST data and gravity gradients collected along all three axes, they also showed the YY gradient values contributed the most to sectoral and near-sectoral tesseral values [22].

It is because of this way in which the QGG and SST data complement each other - each contributing to sections of the spherical harmonic field the other can not - that a future mission incorporating an atomic interferometer gravity gradiometer must retain the ability to collect SST data. While the QGG data will provide never before collected information about the Earth's time variable gravity field, the SST data will still be needed to properly recover the full gravity field at 450 km.

4.3.3 Gradiometer and Pointing Knowledge Error Results

The following results are compared to a simulation with the specifications of the GRACE-FO mission (no QGG data, O(10μRad pointing error) and

the requirements which were imposed upon the GRACE-FO mission. These requirements are included for reference only - any requirements upon a future hybrid QGG-SST mission are likely to be more stringent. Results at each level of QGG noise are collected with to display performance of each of these error levels and make clear the impact of the pointing knowledge error.

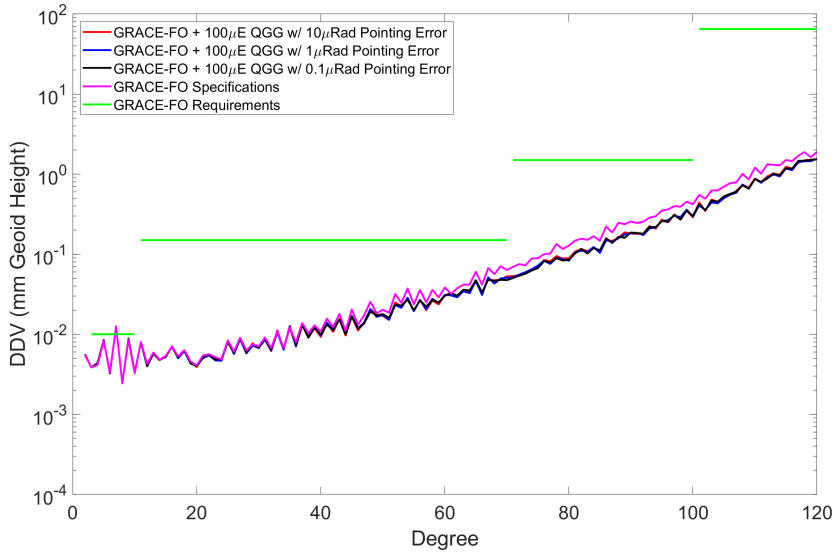

Figure 4.7: Hybrid Architecture with 100μE QGG Noise Simulation Results

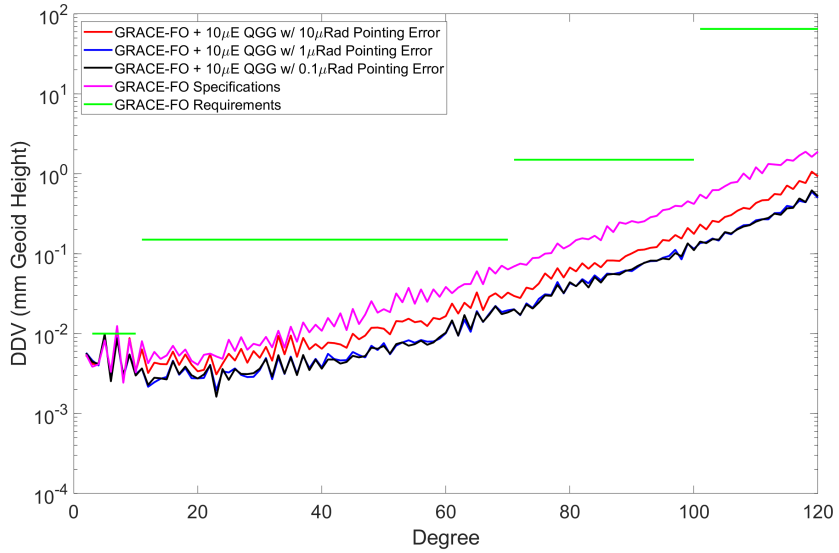

Figure 4.8: Hybrid Architecture with 10μE QGG Noise Simulation Results

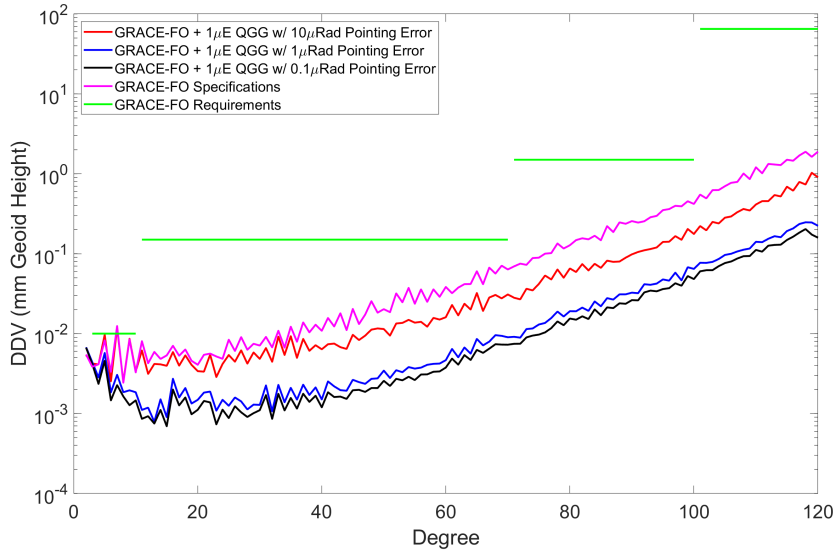

Figure 4.9: Hybrid Architecture with 1μE QGG Noise Simulation Results

It is evident, via figure 4.7, that a hybrid architecture with 100μE QGG noise can make only insignificant improvements upon the performance of the GRACE-FO mission, as expected. At this level of QGG noise, there is no differentiation between the results with varying amounts of pointing knowledge noise. At this noise level, the QGG noise is the limiting factor for improvement.

Performance improves significantly with only 10μE of QGG noise. All simulations in this case perform notably better than GRACE-FO, particularly at medium and high degree spherical harmonics. The cases with 1μRad and 0.1μRad pointing error show improvement over the case with 10μRad pointing error, but are not different from each other. This implies that, with this level of QGG noise, the pointing error is the limiting factor of the performance at 10μRad, but at 0.1μRad, the QGG noise is the limiting factor.

Figure 4.9 shows the simulations with the best case QGG noise, 1μE. The cases with 1μRad and 0.1μRad are noticeably different at this point - with this level of QGG noise, the pointing knowledge is still the limiting factor with a PSD of 1μRad. The absolute best case scenario - 1μE QGG noise and 0.1μRad pointing knowledge noise - has a DDV approximately an entire order of magnitude better than the GRACE-FO case at all medium and high spherical harmonics.

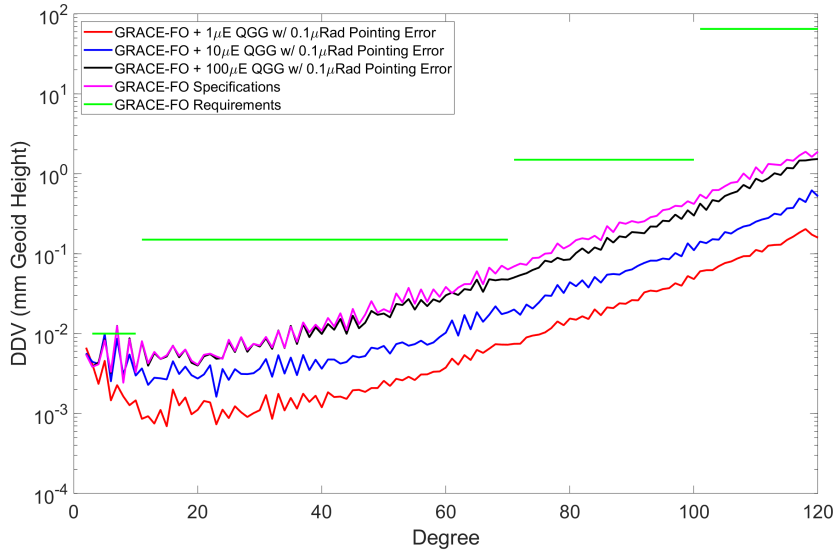

Figure 4.10: Hybrid Architecture with O(0.1μRad) Pointing Knowledge Noise Simulation Results

Figure 4.10, which collects the results of all the simulations with 0.1μRad pointing error, allows for clarity that with this best case pointing knowledge, the QGG error is the limiting factor with both 10 and 100μE noise levels. With the same attitude determination system set to be installed on the IRASSI mission [39], the QGG will be the limiting factor of the mission at all currently achievable levels of QGG noise. Therefore, with this current best case pointing knowledge error, further development of the QGG instrument to 1μE noise or better between the time of this study and the launch of a future hybrid QGG-SST mission will be sufficient for improved overall result accuracy.

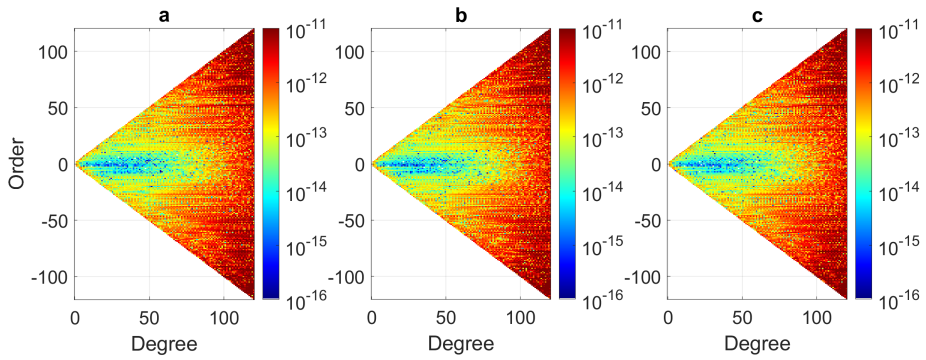

Figure 4.11: Hybrid Architecture with 100μE QGG Noise Simulation Results (Triangle Plots) with (a) 10μRad , (b) 1μRad and (c) 0.1μRad of Pointing Knowledge Noise

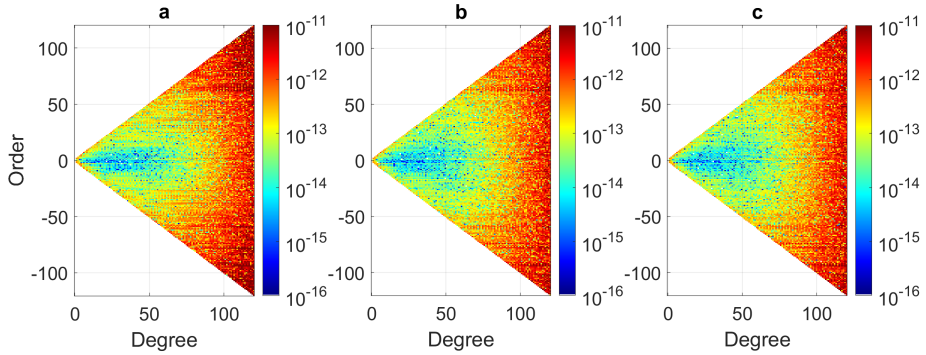

Figure 4.12: Hybrid Architecture with 10μE QGG Noise Simulation Results (Triangle Plots) with (a) 10μRad , (b) 1μRad and (c) 0.1μRad of Pointing Knowledge Noise

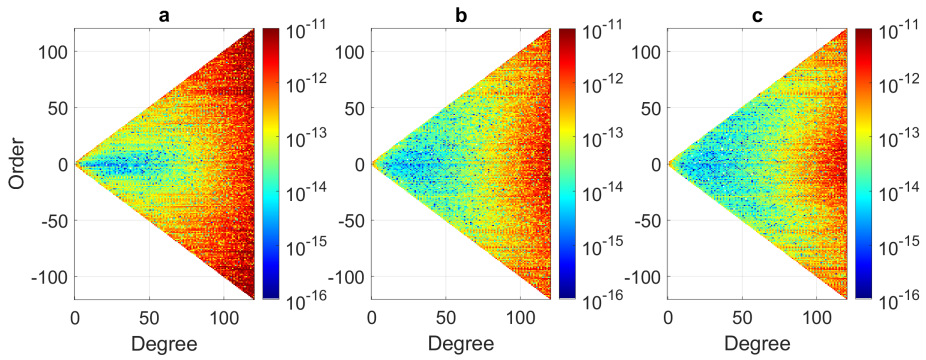

Figure 4.13: Hybrid Architecture with 1μE QGG Noise Simulation Results (Triangle Plots) with (a) 10μRad , (b) 1μRad and (c) 0.1μRad of Pointing Knowledge Noise

The plots in figures 4.11, 4.12 and 4.13 confirm the results and interpretation of figures 4.7, 4.8 and 4.9. Additionally, these plots allow for interpretation of which specific spherical harmonic values move closer to the truth with smaller amounts of QGG and pointing knowledge noise. Improving from 10μRad to 1μRad pointing knowledge error with either 10μE or 1μE QGG error, most major improvements are located at middle degree tesseral and sectoral harmonic values. There is little improvement made at zonal or near-zonal tesseral values, which are well determined in all cases at low and middle degrees. With 1μE QGG noise, an improvement in pointing knowledge from 1μRad to 0.1μRad is accompanied by major improvements in the determination of sectoral and near-sectoral tesseral values at high degrees. As stated previously, improvement with the determination of middle and high

degree values is the goal of the hybrid architecture.

4.3.4 Aliasing Study Results

The information contained in figure 4.14 comes from a series of simulations applying aliasing error through the models described in section 4.2.2. All of these simulations were performed with 1μRad pointing error. One of the simulations contains only SST and GPS data; the other three each contain QGG data, one for each of the QGG noise levels listed in section 4.2.1. The DDV values contained in these plots were calculated after the removal of the ideal correction, the time averaged difference between the true and nominal fields. Therefore, the values in these plots are the aliasing error as described in equation 3.22.

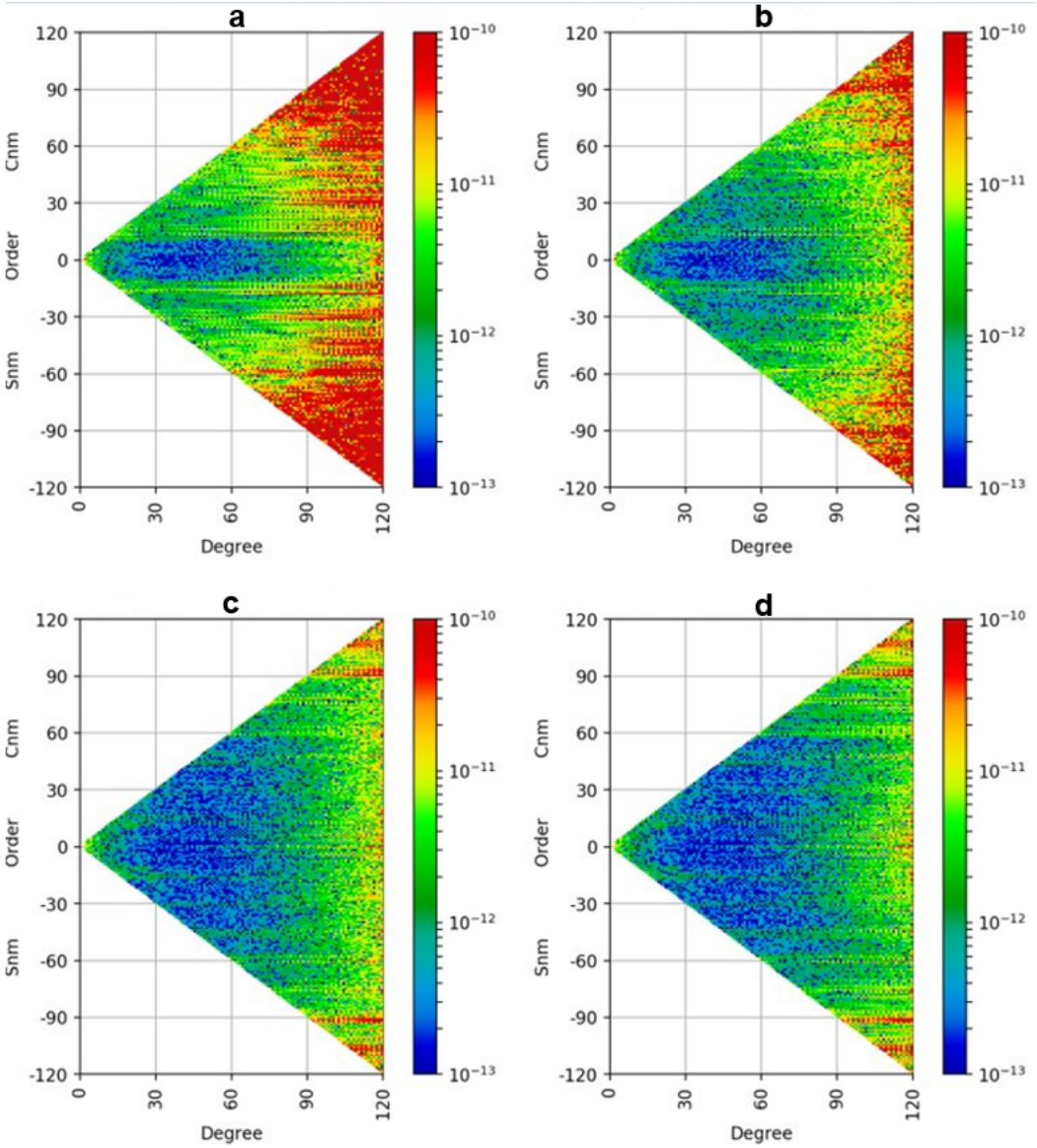

Figure 4.14: Aliasing Error with 1μRad Pointing Error and (a) No QGG Data, (b) QGG Noise 100μE, (c) QGG Noise 10μE and (d) QGG Noise 1μE

Though the aliasing noise is of a larger magnitude than the measure-

ment noise, the pattern of improvement which accompanies improvements in the QGG instrument are the same. Plots b, c and d of figure 4.14 look very similar to the b plots in figures 4.11 through 4.13, which have the same 1μRad pointing noise and descending QGG noise values. There are also some important differences that should be noted. The 100μE case, which added little to the simulations without aliasing, is noticeably better than the SST+GPS case at reducing aliasing noise. It is still the case that major improvements are made in the estimation of high degree sectoral and near-sectoral harmonic values when the QGG noise level decreases from 100μE to 10μE. However, there is very little difference between the cases with 10μE and 1μE QGG noise. In the results at this pointing noise level, this jump in QGG noise made a small but certain notable difference. Aliasing noise appears to cancel out that effect so that, with 1μRad pointing noise, a QGG with 1μE noise does not provide an advantage over one with noise 10μE.

It is interesting to see the striping around spherical harmonic order 15 reduced significantly with the inclusion of the two more accurate levels of QGG data. This striping is due to a resonant frequency of the orbital motion, as sensed by the satellite tracking data. Order 15 (and all multiples of it, though these additional stripes are less visible in plot a) corresponds to a division of the geoid into sectors with a size that matches up with that resonant frequency, reducing the accuracy of estimation at these orders with only SST and GPS data. However, the distance does not correspond to a resonant frequency for the QGG data. Plots c and d in figure 4.14 make clear that accurate QGG

data, in addition to improvements in estimation of sectoral values, drastically reduces this striping effect. It does not completely erase this effect; as the main contribution of the QGG data is concentrated in the high degree sectoral values, it seems that they don't provide quite enough information to completely negate these effects, as the effects are mostly with harmonics nearer to zonal than sectoral.

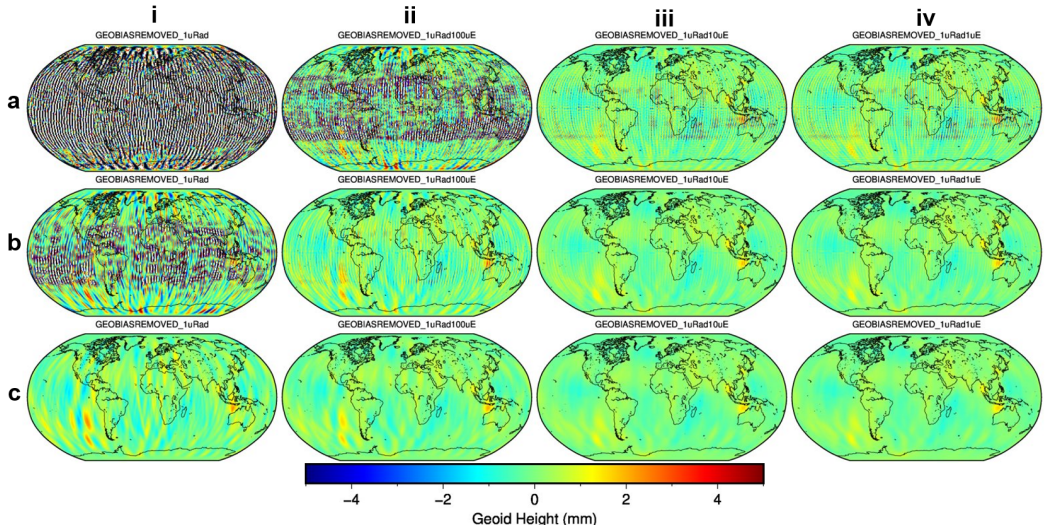

Figure 4.15: Aliasing Error Geoid Height Maps with 1μRad Pointing Error and (i) No QGG Data, (ii) 100μE QGG Noise, (iii) 10μE QGG Noise, (iv) 1μE QGG Noise, Smoothed to (a) 150km, (b) 200km and (c) 300km Resolution

The striping present in figure 4.15 is assessed qualitatively. This reduction in aliasing error created by the inclusion of QGG data allows for smoothing to dealias at finer resolutions. The case with no QGG data included requires a large resolution for the complete removal of striping. Even at the largest

resolution tested, 300km, plot c-i in figure 4.15 still contains notable stripes. However, when QGG data is included with noise levels at either 10 or 1μE, smoothing at resolution 200km is enough to completely remove stripes from plots b-iii and b-iv. With 1μE QGG noise, smoothing at the fine resolution of 150km is enough to remove nearly all striping in plot a-iv.

Smoothing works well to dealias solutions, but it is accompanied by the inherent danger of discarding of useful signal alongside the aliasing error. This danger is particularly relevant to the hybrid architecture mission, which is focused on detecting time variable gravity signals that take occur over small spatial scales; if it were necessary to smooth across large spans to dealias these solutions, it is likely that this desired information would be smoothed out as well. By allowing for dealiasing at finer resolutions, the QGG data makes it more likely that all of the information about the time variable gravity field collected by the mission is retained through this lesser smoothing process.

It is clear to see, generally, that the inclusion of QGG data decreases the amount of aliasing noise present, particularly in sectoral and near-sectoral tesseral values. The exact contribution of SST and QGG are detailed in the following images. As with the contribution analysis in section 4.3.2, the simulations displayed and discussed in the following images all have a pointing error of 1μRad and, when QGG data is included, QGG noise of 1μE.

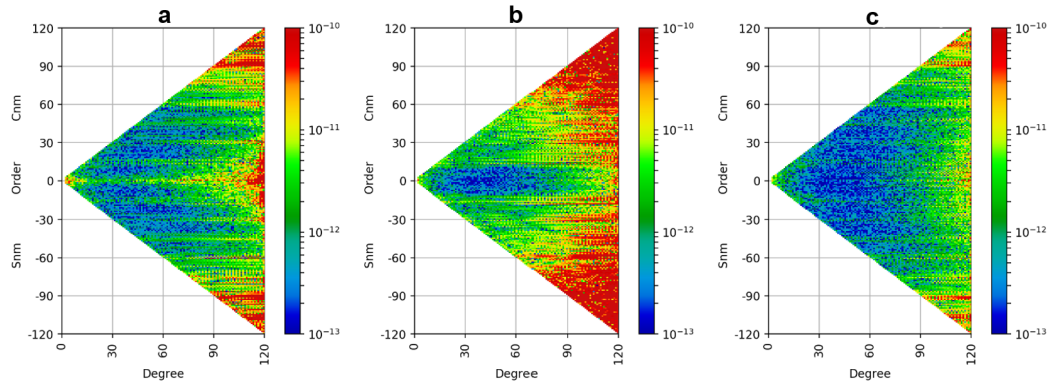

Figure 4.16: All Architecture Type Comparison (Triangle Plots) with Aliasing, (a) QGG+GPS, (b) SST+GPS and (c) SST+QGG+GPS

Displayed in figure 4.16 are the results of differnet architectures with aliasing error applied. These plots bear a resemblance to plots b, c and d from figure 4.5 but present some very noticeable differences. Striping effects due to resonances are far more noticeable in both plots a and b, but damp out significantly in plot c. As the stripes are due to an orbital resonance frequency, it appears that overall the more non-GPS data present, the less significant the striping. The QGG+GPS and SST+GPS cases both perform worse individually than their counterparts without aliasing error at high degrees. The full hybrid architecture, however, appears to maintain an accuracy level at these high degrees that is only moderately worse than its counterpart without aliasing. It is still the case that the QGG+GPS simulation performs best at sectoral and near-sectoral harmonics, and the SST+GPS case still performs best at zonal and near-zonal harmonics

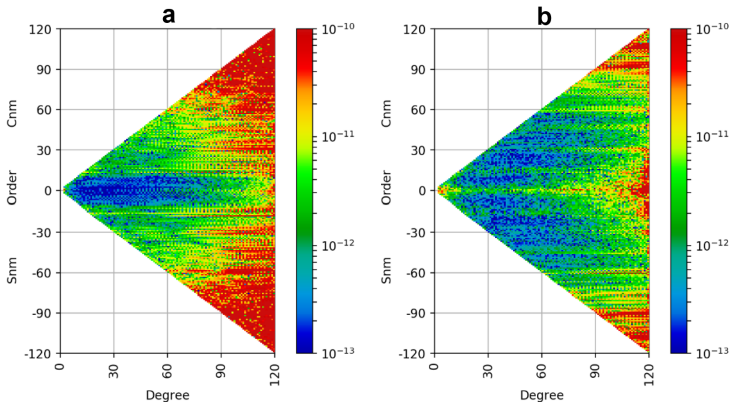

Figure 4.17: Contribution Towards Hybrid Architecture Results with Aliasing from (a) QGG Data and (b) SST Data

As with before, the contributions plots confirm the results of the individual architecture plots. The data in the plots in figure 4.17 is calculated via equation 4.3, with blue indicating a low contribution and red indicating a high contribution. These plots are similar to 4.6, with some of the same differences noted in discussion of 4.16. The performance overall is worse than cases without aliasing error, as expected, but the patterns of performance are the same.

Chapter 5

Conclusions

The study of the movement of water around the Earth is thousands of years old. In the modern era, the continuation of this study is vitally important as we enter a time of climate change unprecedented in the human era. Over the past two decades, advancements in our understanding of time variable elements of the Earth's gravity field provided by the GRACE missions have led the study of the water cycle into the 21^{st} century. This study performs a proof of concept for the continuation of the study of time variable gravity through a hybrid mission architecture which combines the SST with precise gravity gradients measured by a QGG. This study tested the hypothesis that the combination of these two types of data (and GPS) would allow for improved gravity field recovery, in particular with small and medium scale spatial variations. The contributions from each data type and the effects of major sources of error are simulated and analyzed with the architecture in a GRACE-FO like orbit with most instruments maintaining GRACE-FO accuracy levels.

5.1 Summary of Results

As expected, a hybrid architecture was shown to significantly improve gravity field recovery when simulated at an altitude of 450 km; the conclusions discussed in this chapter are valid for this chosen orbit and all of the associated assumptions. This improvement was particularly notable with medium and high degree spherical harmonic values, which correspond directly to medium and small spatial variations, respectively. Without aliasing error, low degree estimates are not improved, as the contribution analysis shows the QGG adding little information in this region, and therefore the architecture has little advantage at degrees below 50. With aliasing error, estimates of coefficients at degrees as low as 20 are improved. The main contributions of the QGG data are in sectoral and near-sectoral tesseral spherical harmonic terms; the majority of contribution to zonal terms continues to come from the SST data. This contribution analysis is evidence of the necessity to pair the QGG on a future mission with SST measurements, as opposed to a mission solely collecting QGG data.

The pointing and gradiometer error analysis confirms that these are the error sources, outside of aliasing, that present the most immediate challenge to the accuracy of the gravity field recovery. The gradiometer, of course, is the main difference between the hybrid mission simulated and the GRACE-FO mission; with too much gradiometer noise present, the mission would be effectively no differnet than GRACE-FO. The pointing knowledge error was shown to be prominent due to its direct impact upon the gradiometer measurements.

Possible levels of attitude determination noise were studied in search of accuracy levels necessary to bring the associated gradient errors to levels similar to QGG noise. This similarity of scaling allows either of these measurements to be the limiting factor for a given simulation with defined noise levels. When gradiometer noise is 100μE, it does not matter what the pointing knowledge accuracy is among the levels tested, as the gradiometer is not accurate enough in itself to make an impact on the estimation of the gravity field. This stands in contrast to a scenario with gradiometer error 1μE; such a gradiometer is accurate enough to force all tested attitude determination methods to be the limiting factor of the mission.

The best noise levels tested for both the gradiometer (1μE) and the attitude determination system (0.1μRad) are both currently developmental. As the benefit target of the gradiometer must take into account what is feasible with the available quality of pointing knowledge and vice versa, the pairings of these best case noise levels with other levels of the other noise type are closely considered. In a scenario in which an attitude determination system with a PSD of $0.1\mu\text{Rad}/\sqrt{Hz}$ is ready but a gradiometer with a PSD of $1\mu\text{E}/\sqrt{Hz}$ is not, this advanced attitude determination would provide little to no advantage over the 1μRad system currently on the IceSAT-2 mission. This is also the case in a scenario in which a 1μE gradiometer is available but a 0.1μRad attitude determination system is not. When aliasing error is included in simulations run with 1μRad pointing error, this is little difference between the cases with 1μE and 10μE gradiometer error, as the aliasing and pointing error combine

to become a limiting factor.

To provide measurements accurate enough to impact the estimation process, the gravity gradiometer must have a very long interrogation time and a very long arm length, given the current state of the technology. While it is feasible to design the instrument in this manner, it is possible that fitting such an instrument on a satellite will create a significant design challenge in the future. It is possible that the technology will be improved in the coming years to allow for similarly accurate measurements at a reduced footprint.

The advantage of pointing the QGG along the orbital cross-track axis confirmed evidence presented by Yi and Rummel [22]. Simulation results showed that the gravity field estimation performed better with the gradiometer pointed along the cross-track; the derivation in section 3.4 explains why this is the case. With this mathematical reasoning and the noise PSDs discussed in section 4.3.1, it is unequivocally clear that the SRF Y-axis is the best option for collecting data with the QGG in order to minimize the effect of pointing error at 450 km altitude.

Finally, the study of aliasing provided evidence that the inclusion of sufficiently accurate QGG data would reduce aliasing error. This error reduction impacted the estimation of both the sectoral and near-sectoral tesseral values, as in the cases without aliasing error, and the stripes at harmonic order 15 and its multiples caused by an SST resonant frequency. This overall reduction in aliasing error allows for the smoothing of the results to be adequate at finer resolutions than needs to be applied to GRACE-FO. Smoothing over

these smaller distances decreases the chance that the smoothing will remove the desired information, the effects of time variable gravity. Given that the hybrid mission is intended specifically to detect time variable effects at smaller spatial scales than GRACE-FO, this finer smoothing resolution is particularly important, and again shows that this architecture concept for a future gravity sensing mission would be a significant step forwards from GRACE-FO.

5.2 Recommendation for Future Analysis

As this study is meant to serve only as a proof of measurement concept for a hybrid QGG-SST architecture, it focused only on the major concerns surrounding such an architecture. There are many other details of this architecture - such as the accelerometer, the orbit, the integration of the gradiometer instrument on the satellite, etc. - that will require further investigation before this architecture can be implemented. The assumption that a mission utilizing this architecture would fly with all of these details exactly the same as the GRACE-FO mission served well for investigating the more pertinent details of gradiometer, pointing and aliasing error and the contribution from the data types. However, it is possible that changes in these aspects of the mission, large or small, may prove to provide some amount of benefit which was outside the scope of this study.

The methods by which the simulations in this study were run were at times tedious. These methods fit well within the classical definition of a simulation, allowing for an advanced understanding of how a hybrid architecture

will perform without direct testing. As the industry pivots towards DevOps, wherein the simulations and operations of satellites are performed via software while the engineers focus on the creation of blocks of code which can be reused and reorganized by that software [50], the simulation schema at CSR will prove convenient. MSODP and AESoP are, effectively, already large code blocks of this manner that are developed and maintained by the engineers at CSR. Therefore, a significant step towards DevOps has already been taken by CSR. The main addition necessary for a complete transition is software capable of utilizing these code blocks in the various necessary ways to create the simulations such as those discussed in this study without the intervention of the engineers.

This study demonstrates that a future mission with a hybrid QGG-SST architecture would be a good choice for continuing on from the GRACE missions, maintaining and improving upon their capabilities for detecting time variable gravity and understanding the movement of water across Earth.

Appendices

Appendix A

Least Squares Estimation Algorithm

The AESoP code, designed for use at The Center for Space Research, runs a batch least squares filter to complete the gravity field estimation process. The process is described here, and can be found in greater detail in Tapley [28]. The equations of motion for a satellite are described in equation A.1.

$$\dot{X} = F(X, t), \quad X(t_k) = X_k \tag{A.1}$$

where

X is an n-dimensional state vector

F is a non-linear n-dimensional vector function describing the system dynamics

X_0 is an n-dimensional initial state vector

The state is related to the observations, Y (p-dimensions), by a model G. The observations are discretized. Error ϵ is introduced as the model is not a completely perfect representation of the relationship between the state and the observations.

$$Y_i = G(X_i, t_i) + \epsilon_i, \quad i = 1, ...l \tag{A.2}$$

Generally speaking, $p < n$. m, the total number of observations, is equal to $p \times l > n$ [28]. To allow for proper linearization, it is best for the nominal trajectory X to be close to the reference trajectory X^* throughout the entire time period during which observations are made. This allows for expanding the motion of the satellite into a Taylor series over the course of its trajectory about the reference trajectory, thus describing the motion as a set of differential equations. This method can be used to create a linear relationship between the state and the observations. Differencing the nominal trajectory and the reference trajectory determines the deviations from the reference trajectory; successive iterations of changing the state parameters ideally lead to the deviations getting smaller, eventually producing a converged orbit resembling the reference trajectory [30]. Models for these deviations can be described as in equation A.3.

$$x(t) = X(t) - X^*(t), \quad y(t) = Y(t) - Y^*(t) \tag{A.3}$$

Substituting the parts of equation A.3 into equations A.1 and A.2 allows them to be functions of the deviations in the state and observations, respectively. Taylor series expansion and truncation by remomving higher order terms (under the assumption that those terms are much smaller than the first order terms) allows for these formulas to become linear approximations,

as mentioned above [28].

$$\begin{aligned} \dot{x}(t) &= A(t)x, \quad x(t_k) = x(k) \\ y_i &= \bar{H}_i x_i + \epsilon, \quad i = 1, ...k \end{aligned} \tag{A.4}$$

$\bar{H}_i$ is a $p \times n$ dimensional linear relation between the state and observation at time i

$$A(t) = \frac{\partial F(X^*, t)}{\partial X} \tag{A.5}$$

$$\bar{H}_i = \frac{\partial G(X^*, t)}{\partial X} \tag{A.6}$$

This completes the replacement of the original non-linear problem with an approximately equivalent linear estimation problem. The state can be propagated as shown in equation A.7. The state transition matrix, used in propagation, is defined by equation A.8.

$$x(t) = \Phi(t, t_k)x_k \tag{A.7}$$

$$\dot{\Phi}(t, t_k) = A(t)\Phi(t, t_0), \quad \Phi(t_k, t_k) = I \tag{A.8}$$

All parts i of the observation component of equation A.4 are consolidated into equation A.9.

$$y = Hx_k + \epsilon, \quad y = \begin{bmatrix} y_1 \\ \vdots \\ y_l \end{bmatrix}, \quad H = \begin{bmatrix} \bar{H}_1\Phi(t_1, t_k) \\ \vdots \\ \bar{H}_l\Phi(t_l, t_k) \end{bmatrix}, \quad \epsilon = \begin{bmatrix} \epsilon_1 \\ \vdots \\ \epsilon_l \end{bmatrix} \tag{A.9}$$

y and ϵ are $m \times 1$ vectors, x_k is an $n \times 1$ vector and H is an $m \times n$ mapping matrix. This is a system of m equations with n unknowns; because in this study there are more observations than estimated parameters (as with most orbit determination problems) the system is over-determined.

Given the intention to find an estimate of the state x so that the error is minimized, the performance index described in equation A.10 is utilized [51, 52].

$$J(x) = \frac{1}{2}\epsilon^T\epsilon \tag{A.10}$$

Substituting equation A.9 into equation A.10 yields the following expression for the performance index.

$$J(x) = \frac{1}{2}(y - Hx)^T(y - Hx) \tag{A.11}$$

The conditions for a unique minimum of this expression are described in equation A.12.

$$\frac{\partial J}{\partial x} = 0, \quad \delta x^T \frac{\partial^2 J}{\partial x^2}\delta x > 0 \tag{A.12}$$

for all $\delta x \neq 0$. Due to the second (sufficient) condition in equation A.12, it is evident that the second derivative of J must be positive definite. Determining the full expression for conditions described in equation A.12 with equation A.11 yields the following.

$$\frac{\partial J}{\partial x} = -(y - Hx)^T H = 0 \tag{A.13}$$

$$\frac{\partial^J}{\partial x^2} = H^T H \tag{A.14}$$

With the sufficient condition met in equation A.14 as long as H is full rank, equation A.13 can be rearranged to show the best estimate of the state, $\hat{x}$, is as given in equation A.15.

$$\hat{x}_k = (H^T H)^{-1} H^T y \tag{A.15}$$

However, as some observations are preferred over others, it is necessary to introduce a method for weighting some over others. This is done by introducing an associated weighting matrix, W, into the performance index in equation A.10.

$$J = \frac{1}{2} \epsilon^T W \epsilon \tag{A.16}$$

where W is a diagonal matrix of dimensions $l \times l$. The values along the diagonal, w_i, are values between 0 and 1, representing the weight given to

observation i. The new formulation of the least squares solution then becomes the following.

$$\hat{x}_k = (H^T W H)^{-1} H^T W y = P_k H^T W y \tag{A.17}$$

where

P_k is the variance-covariance matrix (so long as W is properly selected)

P_k is a representation of the accuracy of the estimate $\hat{x}_k$. Larger values in P_k imply a less accurate estimate.

Bibliography

[1] Byron D. Tapley et al. Contributions of GRACE to Understanding Climate Change. *Nature Climate Change*, 9:358–369, May 2019.

[2] Towards a sustained observing system for mass transport to understand global change and to benefit society. May 2016.

[3] Richard P. Kornfeld et al. GRACE-FO: The Gravity Recovery and Climate Experiment Follow-On Mission. *Journal of Spacecraft and Rockets*, 56(3), May-June 2019.

[4] N. Yu and J.M. Kohel et al. Development of an Atom-Interferometer Gravity Gradiometer for Gravity Measurement from Space. *Applied Physics*, 84:647–652, July 2006.

[5] Robert Shapiro and Dirk Schulze-Makuch. The Search for Alien Life in our Solar System: Strategies and Priorities. *Astrobiology*, 9(4):335–343, 2009.

[6] C.V. Sreenivasa Ayyangar. *Yuddhakanda*. The Little Flower Co., Madras, 1991.

[7] David Deming. Born to Trouble: Bernard Palissy and the Hydrologic Cycle. *Ground Water*, 43(6):969–972, November-December 2005.

[8] Richard W. Katz. Sir Gilbert Walker and a Connection between El Niño and Statistics. *Statistical Science*, 17(1):97–112, 2002.

[9] Krzysztof Sośnica et al. Time Variable Earth's Gravity Field from SLR Satellites. *J Geod*, 89:945–960, 2015.

[10] Moritz Rexer et al. *Gravity, Geoid and Height Systems*. 2014.

[11] Michel Van Camp et al. Geophysics from Terrestrial Time-Variable Gravity Measurements. *Reviews of Geophysics*, 55(4):938–992, September 2017.

[12] Byron Tapley et al. *Contributions of Space Geodesy to Geodynamics: Earth Dynamics*, volume 24. January 1993.

[13] R. S. Nerem et al. Observations of Annual Variations of the Earth's Gravitational Field Using Satellite Laser Ranging and Geophysical Models. *Geophysical Research Letters*, 27(12):1783–1786, June 2000.

[14] Rolf König et al. SLR and the CHAMP Gravity Field Mission. *International Workshop on Laser Ranging*, 13, 2002.

[15] P.F. Thompson. *Interpreting the Earth's time varying geopotential as observed from space and comparisons to global models of hydrologic transport*. PhD dissertation, The University of Texas at Austin, 2004.

[16] Enrico Kurtenbach. Deriving daily snapshots of the Earth's gravity field from GRACE L1B data using Kalman filtering. *Geophysical Research Letters*, 36(17), September 2009.

[17] Felix W. Landerer et al. Extending the Global Mass Change Data Record: GRACE Follow-On Instrument and Science Data Performance. *Geophysical Research Letters*, 47(12), May 2020.

[18] N. Pie et al. Time Variable Earth Gravity Field Models from the First Spaceborne Laser Ranging Interferometer. *Jour. Geophys. Res. in review.*

[19] R. Rummel. GOCE: Gravitational Gradiometry in a Satellite, 2010. Handbook of Geomathematics.

[20] Reports for Mission Selection: The Four Candidate Earth Explorer Core Missions. July 1999. Report Prepared by Earth Sciences Division, Earth Observation Preparatory Division.

[21] Th. Gruber, R. Rummel, O. Abrikosov, and R. van Hees. GOCE High Level Processing Facility: GOCE Level 2 Product Data Handbook, April 2014.

[22] Weiyong Yi and Reiner Rummel. CONTRIBUTION ANALYSIS OF THE GRAVITY FIELD RECOVERED FROM GOCE. 2011. Proceedings of the 4th International GOCE User Workshop, ESA Publication SP-696.

[23] H. Hashemi Farahani et al. The static gravity field model DGM-1S from GRACE and GOCE data: computation, validation and an analysis of GOCE mission's added value. 87:843–867, July 2013.

[24] Thriving on Our Changing Planet: A Decadal Strategy for Earth Observation from Space. 2018. A Consensus Study Report of the National Academies Science, Engineering and Medicine.

[25] Charles Dunn et al. Instrument of GRACE: GPS Augments Gravity Measurements, February 2003.

[26] S. Bettadpur. Gravity Recovery and Climate Experiment Level-2 Gravity Field Product User Handbook, April 2018.

[27] W.M. Kaula. Theory of Satellite Geodesy: Applications of Satellites to Geodesy. 2000.

[28] B.D. Tapley et al. Satellite Orbit Determination. 2004.

[29] Björn Frommknecht et al. GOCE Level 1b Data Processing. *J Geod*, 85:759–775, June 2011.

[30] H.J. Rim and Peter Nagel. Using MSODP. June 2002.

[31] B.C. Gunter. *Computational Methods and Processing Strategies for Estimations Earth's Gravity Field*. PhD dissertation, Department of Aerospace Engineering and Engineering Mechanics, The University of Texas at Austin, December 2004.

[32] W.A. Heiskanen and H. Moritz. Physical Geodesy. 1967.

[33] J. Kim. *Simulation Study of a Low-Low Satellite-to-Satellite Tracking Mission*. PhD dissertation, Department of Aerospace Engineering and Engineering Mechanics, The University of Texas at Austin, May 2000.

[34] Z. Kang et al. GRACE-FO Precise Orbit Determination and Gravtiy Recovery. *Journal of Geodesy*, 94(85), August 2020.

[35] S. Bettadpur and C. McCullough. *Global Gravity Field MOdeling from Satellite-to-Satellite Tracking Data*. Springer International Publishing, 2017.

[36] Sheng wey Chiow, November 2020. Private Communication.

[37] Srvinivas V. Bettadpur, Bob E. Schutz, and John B. Lundberg. Spherical Harmonic Synthesis and Least Squares Computations in Satellite Gravity Gradiometry. *Bulletin Géodésique*, pages 261–271, March 1992.

[38] S. Bae, B. Helgeson, and M. James et al. Performance of ICESat-2 Precision Pointing Determination. *Earth and Space Science*, 8(4), February 2021.

[39] D. Bhatia et al. High Accuracy Pointing Attitude Determination Estimator System of the Future Infrared Astronomy Satellite Swarm Mission. 10^{th} *International ESA Conference on Guidance, Navigation & Control Systems*, May 2017.

[40] R. Ray et al. Diurnal and Semidiurnal Variations in the Earth's Rotation Rate Induced by Ocean Tides. *Science*, 264:830–832, 1994.

[41] F. Lefevre et al. FES2004 Model (realization FES2004_r190105). 2005.

[42] Henryk Dobslaw et al. Gravity Recovery and Climate Experiment: Product Description for AOD1B Release 06, October 2017.

[43] Tatyana Pekker, July 2021. Private Communication.

[44] Observing the Pole Tide with Satellite Altimetry. *Journal of Geophysical Research*, 107, 2002.

[45] C.F. Sakumura. *The Framework for Satellite Gravity Data Assimilation into Land Surface Models*. PhD dissertation, Department of Aerospace Engineering and Engineering Mechanics, The University of Texas at Austin, May 2016.

[46] Srinivas Bettadpur, July 2021. Private Communication.

[47] Srinivas Bettadpur. Gravity Recovery and Climate Experiment: UTCSR Level-2 Processing Standards Document, April 2018.

[48] M. Rodell et al. The Global Land Data Assimilation System. *American Meteorology Society*, 277:381–394, June 2003.

[49] Maxon Widner. *Expected Improvements in Modeling Earth's Time-Variable Gravity Field Using Multiple GRACE-Like Satellite Constellations*. Master's thesis, The University of Texas at Austin, 2018.

[50] Simon Halpern. Op-Ed — Is the Future of Space Ops Officeless? July 2020.

[51] Solving Least Squares Problem. 1974.

[52] NUmerical Methods for Least Squares Problems. 1996.

[53] J.B. Thomas. An Analysis of Gravity-Field Estimation Based on Intersatellite Dual-1-Way Biased Ranging. *JPL Publication*, 98(15), May 1999.